APPLICATION OF THE SDC OPTIMAL CONTROL ALGORITHM TO LOW-THRUST ESCAPE AND CAPTURE TRAJECTORY OPTIMIZATION

Gregory J. Whiffen[1] and Jon A. Sims[1]

An application of the new optimization algorithm called Static/Dynamic Control (SDC) to design low-thrust escape and capture trajectories is presented. SDC is a general optimization method that is distinct from both parameter optimization and the calculus of variations. Trajectories are integrated with a multi-body force model and feature solar electric propulsion with a specific impulse that is a function of the engine throttle. The test problems include interplanetary scale trajectories that capture or escape at one of the inner planets. Optimizing capture and escape trajectories with a multi-body force model results in a significant improvement in the mass delivered compared to existing two-body formulations. SDC is robust for this application and does not require a good initial guess.

INTRODUCTION

Low-thrust electric propulsion is increasingly being selected as the propulsion system of choice for future interplanetary missions. The higher efficiency of electric propulsion compared to traditional chemical propulsion results in larger payload delivered or shorter flight times. The successful Deep Space 1 mission demonstrated the reliability of electric propulsion.

Optimizing low-thrust trajectories, and in particular, trajectories that include escape and capture is inherently difficult. Low thrust engines typically operate for days, months or even years. This is in contrast to chemical systems that operate for minutes. The continuous operation associated with low thrust significantly increases the optimization complexity. Continuous thrust renders approximations and tools used for chemical propulsion (and ballistic) trajectories inaccurate or useless. High fidelity modeling of escape and capture requires a multi-body force model. However, a multi-body force model will only further compound the optimization complexity. To fully optimize an escape or capture trajectory, the origin or destination of the trajectory must be taken into account. Typically this involves an interplanetary scale trajectory leg. However, optimizing a trajectory involving both an interplanetary leg and a planet centered spiral introduces two very different time and distance scales into mathematical formulation. Widely varying time and distance scales are known to create difficulty for optimization.

Previous work sought to avoid many of the aforementioned difficulties by using a two-body approximation and/or a divide and conquer approach for escape and capture[7]. For example, an Earth to Mars capture trajectory can be approximated as two separate problems. First, an optimal interplanetary trajectory from Earth to Mars is obtained such that the incoming V_∞ at Mars is zero. Second, a Mars centered spiral problem is solved (with only Mars gravitating). The spiral problem begins with two-body energy of zero and ends with the target capture orbit around Mars. Although Two-body formulations are much simpler to solve, they do not take advantage the strong multi-body effects that occur near zero energy, and they can not optimize the trajectory end-to-end.

[1]Member of the Engineering Staff, Navigation and Flight Mechanics Section, Jet Propulsion Laboratory, California Institute of Technology, Pasadena, CA 91109

The high fidelity optimization of low-thrust escape and capture with a multi-body force model is the main objective of this research. It is also an objective of this research to optimize trajectories that involve both an interplanetary leg and planet centered spirals without dividing the trajectory up into subproblems (based on length and time scales) and optimizing each independently.

APPROACH

Existing methods for optimizing low-thrust trajectories are classified as either direct or indirect. Direct approaches parameterize the trajectory and solve the parameterized problem using a gradient based nonlinear programming method, or a hueristic method such as simulated annealing. Direct methods typically remove the explicit time dependence in the optimal formulation by parametrizing the trajectory as a series of impulse burns and conic coasts. Indirect approaches are based on the calculus of variations, resulting in a two point boundary value problem[1]. Indirect methods do not remove the explicit time dependence of the trajectory problem, rather it is solved as an optimal control problem. Calculus of variations methods are usually limited to a single body (Sun or planet) force model due to the sensitivity of the method. Intermediate planetary flybys can be modeled by instantaneous rotations of the velocity vector.

The optimization method used in this research is called Static/Dynamic Control or SDC[8]. SDC is a new, general optimization algorithm which was derived to address a general class of problems with the same structure as low-thrust optimization. SDC best fits into the direct method category. However, unlike other direct methods, the explicit time dependence of the optimization problem is not removed by parameterization. The SDC optimization algorithm is a form of optimal control. Unlike many other optimization approaches, SDC can be used with the highest fidelity space flight simulators available.

SDC is a robust optimization method that can handle the large changes in length and time scales that occur in problems with both interplanetary legs and planet centered spirals. In the process of performing this research, it was found that SDC is capable of optimizing end-to-end trajectories with an escape spiral at one planet, followed by an interplanetary leg, and ending with a capture spiral at a second planet.

SDC does not require a good guess to begin the optimization. It is this feature that is used to explore the complex optima space of capture and escape. A large number of poor initial guesses and different initial conditions were generated to begin separate optimizations. The purpose of this procedure is to investigate (with as little bias as possible) the range of available, locally optimal trajectories. Hundreds of different optimal escape and capture trajectories were obtained in this way. A classification system was developed and all trajectories were classified as to one of several distinct minima types. Escape and capture exhibits a symmetry in that, most escape minima types have analogous capture minima types.

The trajectories considered include Earth launch to capture into various orbits at Mars, escape from a fixed high Earth orbit to capture into Mars circular orbits at various altitudes, Earth launch to Venus flyby to capture into various orbits around Mercury, Earth launch to capture into various orbits around Venus, escape from a fixed, high Mars orbit to capture into various Earth orbits, and escape from various high Earth orbits to a rendezvous with Mars. Whenever possible, two-body optimization performance results are compared to multi-body results.

The General SDC Problem Structure

SDC is a general optimization method designed to solve a class of mathematical problems. The SDC optimization algorithm is based in part on the Hamilton, Bellman, Jacobi dynamic programming equation[2]. Unlike traditional differential dynamic programming methods, SDC is constructed

to solve highly nonlinear and non-convex problems with a dual dynamic and parametric structure. Optimal solutions generated by SDC satisfy both the necessary and sufficient conditions of optimality.

Three distinct classes of variables are recognized by SDC. The first is the *dynamic control* which are functions of time. Dynamic control variables are analogous to control variables in optimal control theory. The vector $v(t)$ is used to represent the dynamic control at time t. The second variable class is the *static control* which can be thought of as parameters in the ordinary parameter optimization sense. The vector w is used to represent the static control. Both the static and dynamic control variables encompass design variables that are under direct control by the engineer. In addition to the static and dynamic controls, SDC recognizes time dependent *state* variables. The state vector encompasses variables not under the direct control of the engineer. The vector $x(t)$ is used to represent the state at time t.

The general objective or cost function of SDC can be written as the addition of a time-integrated cost and a sum of point-in-time costs:

$$J = \int_{t_0}^{t_N} F(x(t), v(t), w, t)dt + \sum_{i=1}^{N} G(x(t_i), v(t_i), w, t_i, i). \tag{1}$$

The goal of SDC is to optimize J by choosing the optimal or "best" dynamic control vector $v(t)$ at all time instants $t \in (t_0, t_N)$ simultaneously with the optimal static parameter vector w. The objective J can be either minimized or maximized in value. The general functions F and G in Eq. (1) are selected to best represent the design and control objectives for a specific application. The times t_i are assumed to lie between t_0 and t_N for $i = 1, 2, ..., N-1$. The functions F and G are required to be twice continuously differentiable with respect to x, v, and w. The functions F and G do not need to be continuous in time t.

In addition to the objective Eq. (1), SDC requires an ordinary differential equation which describes the time evolution of the state vector x, and a function that specifies the initial state $x(t = t_0)$:

$$\frac{dx(t)}{dt} = T(x(t), v(t), w, t) \qquad x(t = t_0) = \Gamma(w), \tag{2}$$

The state function T is required to be twice continuously differentiable with respect to x, v, and w. However, the state function T does not need to be continuous in time t. The vector function T is selected to best represent the time evolution of the state vector $x(t)$ under the influence of the current state, the current dynamic control vector $v(t)$, and the static parameter vector w at time instant t. The initial condition can be given and fixed, or it can be a function of the static control vector w. The function Γ is required to be once continuously differentiable with respect to w.

SDC optionally allows two types of constraints on the formulation Eqs. (1) and (2). The first type are ordinary constraints of the general form:

$$L(x(t), v(t), w, t) \geq 0 \quad \textit{and/or} \quad K(x(t), v(t), w, t) = 0, \tag{3}$$

The linear or nonlinear vector functions L and K are selected to represent practical or physical constraints on the engineering problem. An example of a constraint of this type is a minimum allowed distance between the Sun and a spacecraft to avoid spacecraft overheating.

The second type of constraint SDC allows are "control dynamic" constraints. Control dynamic constraints represent any physical or practical engineering constraints on the *time evolution* of the

dynamic control vector $v(t)$. The control dynamic constraints have the general form:

$$v(t) = \left| \begin{array}{ll} f(u_1, w, t, 1) & for \;\; t = t_0 \;\; to \;\; t_1 \\ f(u_2, w, t, 2) & for \;\; t = t_1 \;\; to \;\; t_2 \\ \vdots & \vdots \\ f(u_N, w, t, N) & for \;\; t = t_{N-1} \;\; to \;\; t_N. \end{array} \right| \tag{4}$$

The vector functions $f(u_i, w, t, i)$ are selected to properly represent the limitations on the time evolution of $v(t)$. The number of periods N may be chosen arbitrarily. The functions f are parameterized by a parameter vector u_i, the static parameter vector w, and time t. The functions f can be used to effectively limit or constrain the SDC algorithm to consider only solutions $v(t)$ which are of the form of Eq. (4). The time intervals t_i to t_{i+1} are called "periods." The dynamic parameter vector u_i is constant within each period i, $i = 1, 2, ..., N$. For example, the simplest useful set of functions f is $f(u_i, w, t, i) = u_i$. The dynamic control vector $v(t)$ may be optimized such that $v(t)$ is constant over each period, allowing changes only at period interfaces t_i. Alternatively, $v(t)$ may be subject to a dynamic limitation that allows $v(t)$ to vary within each period, either continuously or discontinuously.

If SDC is used with control dynamic constraints, then the algorithm is called the *period formulation of the SDC*. If no control dynamic constraint is used then the algorithm is called the *fully continuous formulation of SDC*. In this research, the period formulation of SDC was used to constrain the trajectory optimization to only allow changes in the thrust direction and magnitude at regular time intervals. The regular time intervals represent the practical limitations of spacecraft control resulting from communications and/or duty cycles.

Application of SDC to Trajectory Optimization

The first step in applying SDC to the problem of low-thrust trajectory optimization requires defining the state and control variables. The state vector $x(t)$ is defined to be the spacecraft state at any given time t. The components of the state vector $x(t)$ are defined as follows,

$$x(t) = \left[\begin{array}{l} x_1(t) \\ x_2(t) \\ x_3(t) \\ x_4(t) \\ x_5(t) \\ x_6(t) \\ x_7(t) \end{array} \right] = \left[\begin{array}{l} x \; coordinate \; of \; spacecraft \\ y \; coordinate \; of \; spacecraft \\ z \; coordinate \; of \; spacecraft \\ x \; velocity \; of \; spacecraft \\ y \; velocity \; of \; spacecraft \\ z \; velocity \; of \; spacecraft \\ mass \; of \; the \; spacecraft. \end{array} \right] \tag{5}$$

The dynamic control $v(t)$ is defined to be the electric propulsion thrust vector as a function of time. The components of the dynamic control vector $v(t)$ are defined as follows,

$$v(t) = \left[\begin{array}{l} v_1(t) \\ v_2(t) \\ v_3(t) \end{array} \right] = \left[\begin{array}{l} x \; component \; of \; thrust \\ y \; component \; of \; thrust \\ z \; component \; of \; thrust. \end{array} \right] \tag{6}$$

The components of the static control vector w are defined to be

$$w = \begin{bmatrix} w_1 \\ w_2 \\ w_3 \\ w_4 \\ w_5 \\ w_6 \\ \vdots \\ w_{5+n} \end{bmatrix} = \begin{bmatrix} Date\ of\ Earth\ launch \\ total\ flight\ time \\ x\ component\ of\ launch\ V_\infty \\ y\ component\ of\ launch\ V_\infty \\ z\ component\ of\ launch\ V_\infty. \\ Date\ of\ first\ intermediate\ flyby \\ \vdots \\ Date\ of\ n^{th}\ intermediate\ flyby. \end{bmatrix} \tag{7}$$

The SDC algorithm is not limited to the definition Eqs. (5), (6), and (7). These definitions were used to perform comparisons between SDC and existing programs. Additional control and state dimensions can be added. For example, the static control w could be augmented with design parameters like solar array size. The state vector x could be augmented with a state representing the total spacecraft radiation dose.

The second step in applying SDC is to provide an initial condition function $x(t_0) = \Gamma(w)$. The following definition is used to provide a launch from Earth as the initial condition. The initial mass of the spacecraft is obtained from a launch vehicle performance curve depending on the launch $V_\infty = (w_3, w_4, w_5)$.

$$\Gamma(w) = \begin{Bmatrix} initial\ position \\ initial\ velocity \\ initial\ mass \end{Bmatrix} = \begin{Bmatrix} X_e(w_1) \\ V_e(w_1) + w_{3:5} \\ mlv_c(w_{3:5}) \end{Bmatrix} \tag{8}$$

The vector functions $X_e(w_1)$ and $V_e(w_1)$ are the Earth's center location and velocity at the launch date w_1. The function $mlv_c(w_{3:5})$ is the launch mass for the launch energy $C_3 = ||w_{3:5}||^2$. The JPL Lunar and Planetary Ephemerides are used to define $X_e(w_1)$ and $V_e(w_1)$. Note that the trajectory begins at the center of a massless Earth. This simplification was necessary to make comparisons with existing two-body low thrust optimization programs which make the same launch approximation. More realistic launch conditions involving multi-body propagation have been successfully incorporated using SDC.

The state equation used to describe the time evolution of the state is

$$\frac{dx}{dt} = T(x, v, w, t) = \begin{bmatrix} x_4(t) \\ x_5(t) \\ x_6(t) \\ \frac{v_1(t)}{x_7(t)} + \sum_{i=1}^{11} \frac{\mu_i r_i(1)}{||r_i||^3} \\ \frac{v_2(t)}{x_7(t)} + \sum_{i=1}^{11} \frac{\mu_i r_i(2)}{||r_i||^3} \\ \frac{v_3(t)}{x_7(t)} + \sum_{i=1}^{11} \frac{\mu_i r_i(3)}{||r_i||^3} \\ \dot{m}(||v||) \end{bmatrix} = \begin{bmatrix} x\ velocity\ of\ spacecraft \\ y\ velocity\ of\ spacecraft \\ z\ velocity\ of\ spacecraft \\ x\ acceleration\ of\ spacecraft \\ y\ acceleration\ of\ spacecraft \\ z\ acceleration\ of\ spacecraft \\ mass\ flow\ rate \end{bmatrix}, \tag{9}$$

The mass flow rate $\dot{m}$ is provided by a polynomial fit to the performance of the NSTAR 30-cm ion thruster[3], a version of which is in operation on Deep Space 1. The specific impulse is not constant, but depends on the engine throttle level.

Constraints of the form of Eq. (3) are used to constrain the thrust and reach intermediate and final target bodies. The maximum thrust is constrained by the performance of the thruster(s) and the power available from the solar array at a given heliocentric radius. The target final state used in this research is either an orbital energy, a circular orbit, or a massless rendezvous type constraint.

The form of the fixed final energy constraint used in this analysis is

$$E_{target} = \frac{v_{rel}^2}{2} - \frac{\mu_{body}}{||r_{rel}||}. \tag{10}$$

The energy E_{target} is the final orbital energy with respect to the target body. The relative velocity between the spacecraft and the target body is $v_{rel} = v_{spacecraft} - v_{body}$ where $v_{spacecraft} = \{x_4(t_N), x_5(t_N), x_6(t_N)\}$. The parameter μ_{body} is the gravitational constant of the target. The variable $r_{rel} = r_{spacecraft} - r_{body}$ is the separation between the spacecraft and target body. When constraint Eq. (10) is enforced, the optimization will generate an optimal trajectory that achieves a specified orbital energy E_{target}. This constraint is equivalent to fixing the semi-major axis, with all other orbital elements free.

The circular orbit constraint used in this analysis is achieved by using three separate constraints of the form of Eq. (3). The first constraint requires the circular orbit radius:

$$||r_{rel}|| = ||r_{spacecraft} - r_{body}|| = R_{target}, \tag{11}$$

where R_{target} is the specified circular orbit radius (scaler). The second constraint requires the relative velocity magnitude between the spacecraft and body is consistent with a circular orbit:

$$||v_{rel}|| = \sqrt{\frac{\mu_{body}}{||r_{rel}||}}. \tag{12}$$

The third constraint requires the relative velocity to be perpendicular to the separation vector:

$$v_{rel} \cdot r_{rel} = 0. \tag{13}$$

The form of the massless rendezvous constraint (two-body capture) is

$$\begin{aligned} x_{1:3}(t_N) &= r_{body} \\ x_{4:6}(t_N) &= v_{body} \end{aligned} \tag{14}$$

where the vector position of the target body r_{body} and the vector velocity v_{body} are given by the DE405 ephemeris. The constraint Eq. (14) is used to approximate capture in two-body models. For example, a capture at Mars can be approximated by using Eq. (14) with a massless Mars. This constraint is used to compare the performance of optimal two-body capture to optimal multi-body capture.

The objective used for all comparisons was to maximize the final spacecraft mass or net mass, i.e. *maximize* $x_7(t_N)$. This objective takes into account the launch vehicle performance and propellant usage.

RESULTS

Earth Launch to Mars Capture Spiral

The Earth launch to Mars capture problem has a fixed launch date of April 22, 2003. The flight time was 280, 300, 320, 350, or 400 days. The launch vehicle used is a Delta 7326-9.5 with a 10% launch vehicle contingency. The launch V_∞ direction and magnitude is free for optimization. A single NSTAR 30-cm ion thruster is available on the spacecraft. The solar array is assumed large enough so that the engine can operate at full power (92.3 mN at 2.6 kw) anywhere between the Earth and Mars. The target orbit at Mars is either a circular orbit with radius 60,000 km, or an orbit with the equivalent energy. The results are compared to the optimal two-body rendezvous. The optimal

two-body rendezvous uses flight times equal to the time of capture for the corresponding optimal multi-body result. For example, when the flight time is fixed at 350 days, the optimal trajectory to a circular orbit around Mars uses 350 days but achieves capture on day 312.56. A fixed flight time of 312.56 days is used to obtain the two-body capture solution (491.36 kg) based on a massless Mars and the constraint Eq. (14).

Table 1

EARTH LAUNCH - MARS CAPTURE

Time of Flight (d)	Mars Orbit Type	Final Mass (kg)	Final orbit ϵ	Capture Day	Capture Mass (kg)	2-Body Capture Mass (kg)	Multi-body Performance Improvement
280	Circular	351.22	0	254.621	357.43	297.65	59.78 kg (20.1%)
280	Fixed E	352.21	0.2934	254.861	358.37	298.49	59.88 kg (20.1%)
300	Circular	415.25	0	269.503	422.72	351.21	71.51 kg (20.4%)
300	Fixed E	417.02	0.4400	269.916	424.45	352.74	71.71 kg (20.3%)
320	Circular	473.10	0	284.817	481.71	408.77	72.94 kg (17.8%)
320	Fixed E	474.48	0.3307	285.359	482.96	410.81	72.15 kg (17.6%)
350	Circular	497.56	0	312.560	506.56	491.36	15.20 kg (3.09%)
350	Fixed E	497.56	0.2655	313.097	506.57	492.03	14.54 kg (2.96%)
400	Circular	500.02	0	338.361	507.79	501.63	6.16 kg (1.23%)
400	Fixed E	500.75	0.57168	339.082	507.67	501.69	5.98 kg (1.19%)

The final mass in Table 1 is the spacecraft mass in orbit around Mars at the end of the flight time. The capture mass in Table 1 is the spacecraft mass at the instant of Mars capture (two-body energy = 0). The value of ϵ is the final orbit eccentricity (zero for constrained circular orbits and non-zero for fixed final energy orbits). In Table 1, optimal multi-body performance is always better than optimal 2-body performance. Further, the advantage increases with shorter flight times to a plateau around 20%. This is easily understood because the gravity of Mars can be used to increase the spacecraft energy with respect to the Sun, helping to match the energy of the orbit of Mars. This "terminal gravity assist" helps meet the rendezvous condition. Despite Mars' small mass, the multi-body solution is significantly better for short flight times.

Notice in Table 1 that all fixed energy final masses are larger than or equal to the circular orbit final masses with the same time of flight. This is expected because the fixed energy solutions allow more freedom in the shape of the final orbit around Mars. First solving for the optimal fixed energy solution will provide a baseline to judge the performance of solutions with more constrained final orbits. In this case, there is only a small penalty for constraining the final orbit around Mars to be circular.

Notice in Table 1 that the eccentricities of the final orbit around Mars for the fixed energy solutions are 0.29, 0.44, 0.33, 0.27, and 0.57 for the flight times of 280, 300, 320, 350, and 400 days respectively. No particular trend in eccentricity verses flight time is apparent. It turns out that the solutions with high eccentricity belong to one class of local minima and the solutions with lower eccentricity belong to a second class. The two minima classes merge as the flight time is reduced. For example, we can expect a local minima solution for the 350 day flight time with eccentricity of about 0.5. A more detailed analysis of the minima classes is addressed in later subsections. Later subsections demonstrates the coexistence of both high and low eccentricity local minima for a wide range of flight times.

Earth Spiral Escape to Mars Capture Spiral

This problem involves a spiral escape from a high Earth orbit, an interplanetary leg to Mars, and a capture and spiral into Mars circular orbits with various radii. Solving this problem demonstrates the ability of SDC to deal with multiple length and time scale changes in a single trajectory. The initial Earth orbit is circular with a radius of 90,000 km. This starting point may be obtained by spiraling out from a much lower Earth orbit. The initial spacecraft mass is 500 kg. and two NSTAR engine G thrusters are available. In all cases the flight time was fixed at 300 days. All the planets and the Earth's Moon are gravitating. No significant lunar flyby occurs in this series of solutions. The usefulness of the Moon for Earth escape is highly dependent on the initial condition. In this case, the single initial condition used was selected so that it is not advantageously timed for lunar interactions. The added complexity of lunar interactions is addressed in later papers. Table 2 summarizes the impact of targeting ever lower circular orbits around Mars, given a fixed total flight time from Earth orbit. Figure 1 is a plot of the optimal trajectory to a circular orbit around Mars with radius 25,000 km. Figure 2 plots the escape and capture portions of the optimal trajectory to a Mars circular orbit of radius 17,000 km.

The Mars spiral is on the order of 10^4 km whereas the interplanetary trajectory from Earth to Mars is on the order of 10^8 km. SDC converges reliably for the complete trajectory despite a scale change of 10,000. The top graph in Figure 3 plots total propellant required for the transfer from Earth orbit to circular orbit at Mars verses the Mars orbit radius. The bottom graph in Figure 3 plots the number of revolutions at Mars verses the Mars orbit radius.

Table 2

EARTH ESCAPE - MARS CAPTURE

Mars Circular Orbit [km]	Propellant Mass [kg]	Revolutions at Mars	Capture Mass [kg]	Capture Day
65,000	94.44	1	412.31	289.97
60,000	95.01	1.2	411.70	287.83
50,000	96.55	1.6	411.04	284.45
40,000	98.96	2.4	409.96	281.72
35,000	100.73	3.1	409.08	279.89
30,000	102.97	4.2	407.87	277.78
25,000	106.06	6.0	406.16	274.97
22,000	108.76	7.6	404.44	272.94
20,000	111.12	9.2	402.87	271.34
18,000	113.98	11.3	400.87	269.58
17,000	115.68	12.5	399.64	268.62
16,000	117.74	14.1	398.11	267.54
15,000	120.15	15.9	396.26	266.37
14,000	123.03	18.2	394.01	265.12

The propellant mass in Table 2 is the total propellant required to achieve the specified circular orbit around Mars beginning in Earth orbit.

Earth Launch to Venus Flyby to Mercury Capture Spiral

This trajectory is well known to be difficult to optimize, even if the Mercury capture spiral is replaced by the simpler two-body rendezvous condition Eq. (14). The Mercury spiral and the heliocentric spiral to reach Mercury introduces two very different scale spirals. Since Mercury is

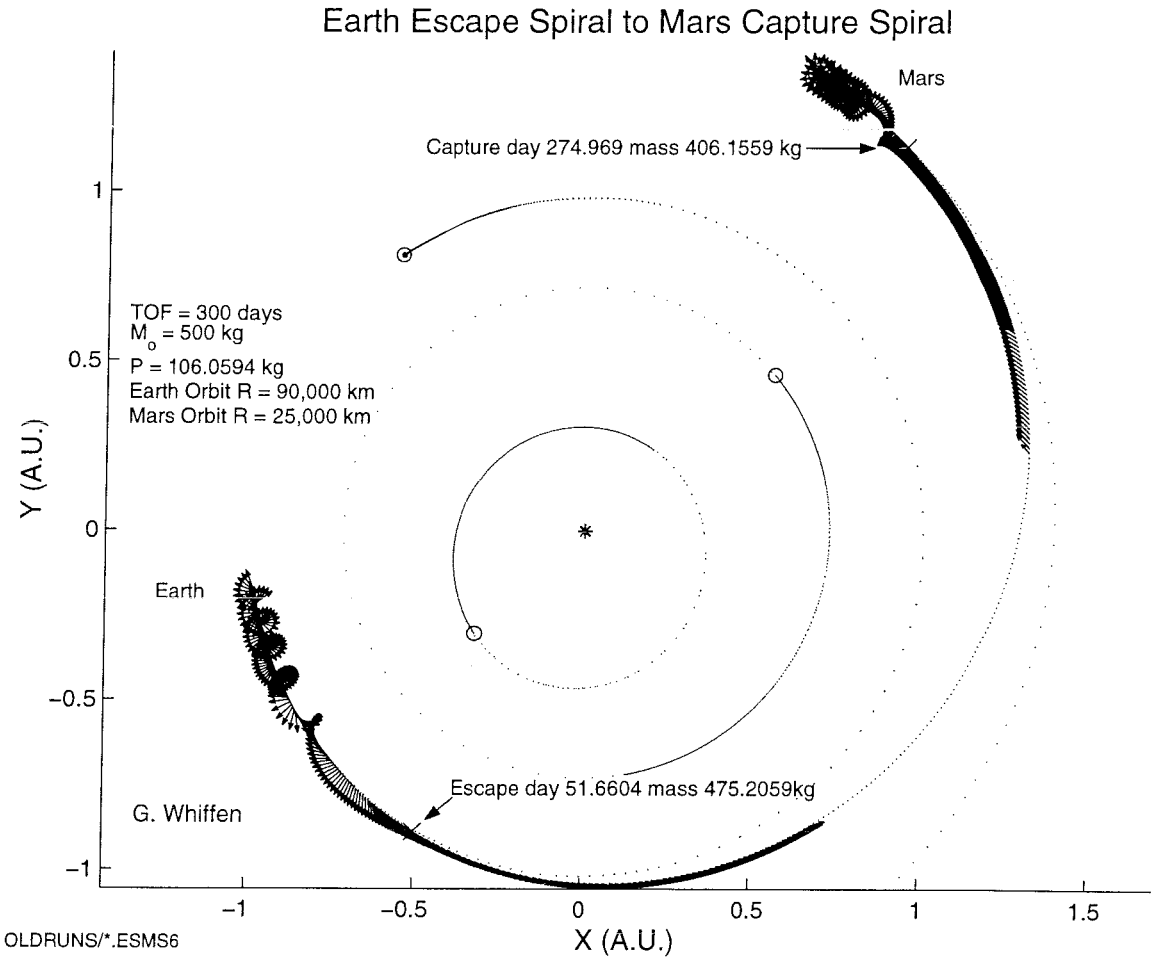

Figure 1: SDC optimal trajectory for the Earth escape spiral to Mars capture spiral problem. The arrows along the spacecraft trajectory indicate the thrust direction. The lack of arrows along the trajectory indicate coasting periods.

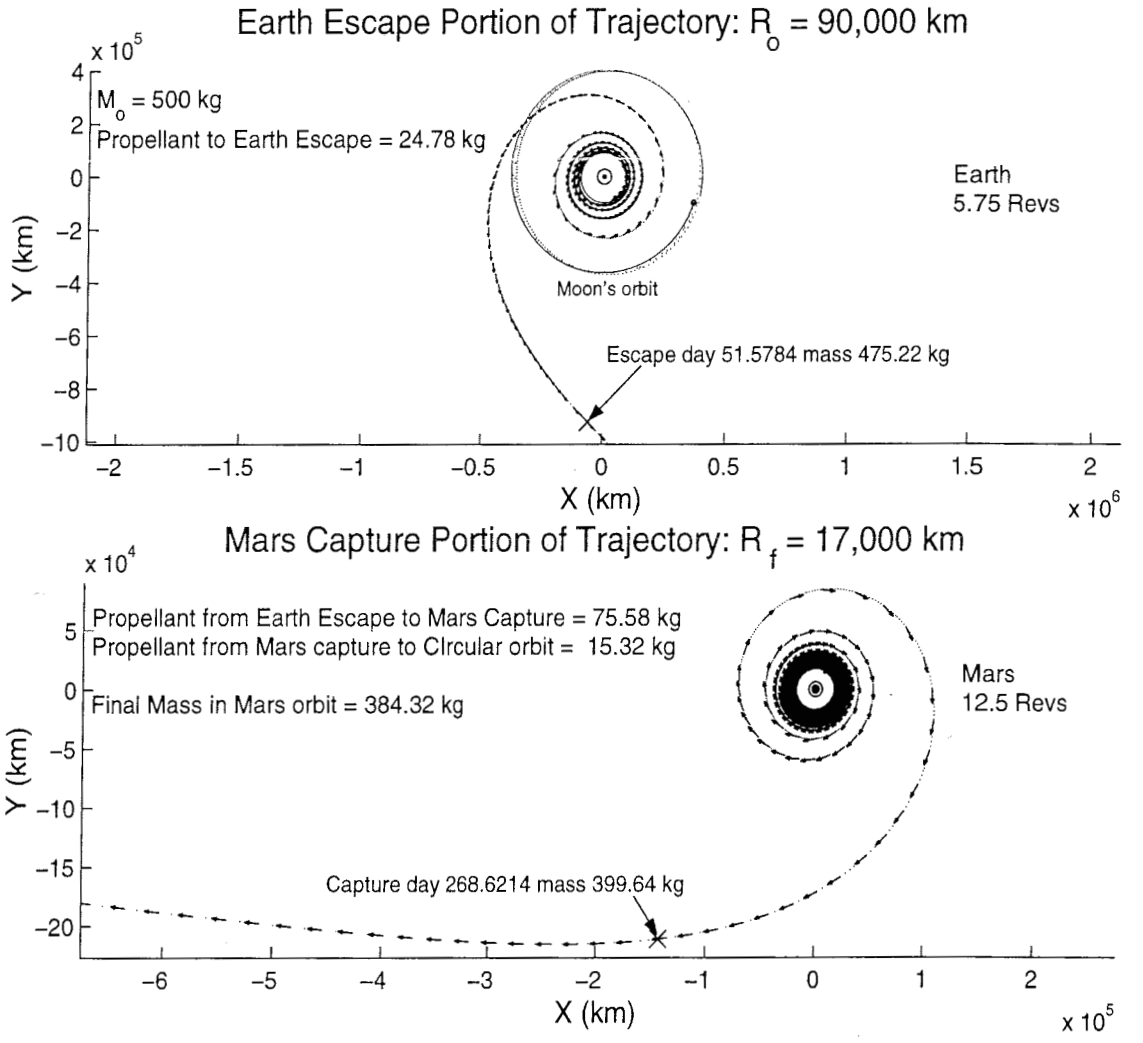

Figure 2: SDC optimal trajectory for the Earth escape spiral to Mars capture spiral problem: Earth escape and Mars capture portions. The final Mars orbit radius is 17,000 km. The arrows along the spacecraft trajectory indicate the thrust direction.

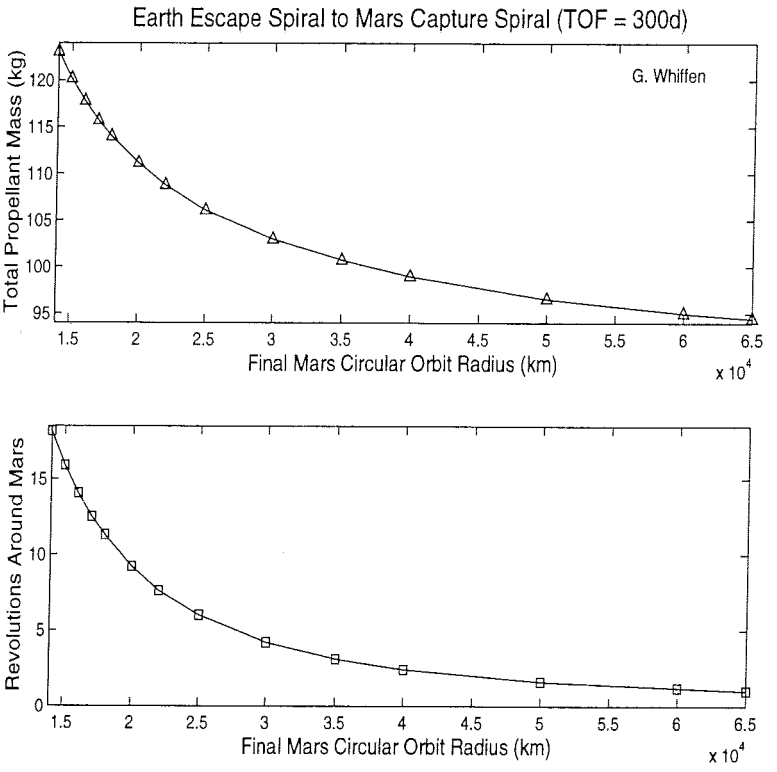

Figure 3: SDC optimal trajectory for the Earth escape spiral to Mars capture spiral problem. Propellant from Earth orbit and revolutions required in Mars orbit are plotted verses the final Mars orbit radius.

less massive than Mars, the advantage of multi-body optimization over two-body optimization is generally smaller than for Mars capture trajectories.

The base case problem requires a launch on August 29, 2002, Venus flyby on February 11, 2003, and arrival in Mercury orbit on December 24, 2004. Other comparisons involve freeing the launch, Venus flyby, and choosing different arrival dates. The launch vehicle used is the Delta 7326-9.5 with a 10% launch vehicle contingency. The launch V_∞ direction and magnitude are free for optimization. A single NSTAR engine G thruster is available on the spacecraft. The power available to the thruster at 1 A.U. is 1.3 kw. With this array, the thruster can operate at its maximum rated power only for heliocentric radii below 0.6455 A.U. At radii above 0.6455 A.U. the engine must be throttled. The base case orbit at Mercury is either a circular orbit with radius 30,000 km, or an orbit with the equivalent energy.

Multi-body capture optimization is compared to two-body capture optimization. The two-body optimization of rendezvous uses flight times equal to the flight time to capture for the corresponding optimal multi-body result. Note that in both the two- and multi-body formulations, the flyby of Venus is integrated using multi-body force laws. The only difference between the two- and multi-body formulations is the mathematical form of the terminal state constraint corresponding to whether or not Mercury is gravitating. Figure 4 is an example of an optimal trajectory to a circular orbit around Mercury of 19,000 km. Table 3 summarizes the results for the base case: launch date, Venus flyby date, and arrival date fixed.

Table 3

EARTH LAUNCH - VENUS FLYBY - MERCURY CAPTURE
Launch Date Fixed and Venus Flyby Date Fixed

Time of Flight (d)	Mercury Orbit Type	Final Mass (kg)	Final Orbit ϵ	Capture Day	Capture Mass (kg)	2-Body Capture Mass (kg)	Multi-body Optimization Improvement
847.325	Circular	319.24	0	826.763	324.27	288.47	35.80 kg (12.4%)
847.325	Fixed E	319.87	0.2843	827.135	324.81	288.98	35.83 kg (12.4%)
857.325	Circular	334.53	0	835.465	339.87	300.69	39.18 kg (13.0%)
857.325	Fixed E	334.65	0.2500	835.449	340.00	300.67	39.33 kg (13.1%)
887.325	Circular	345.35	0	861.888	351.56	333.22	18.34 kg (5.50%)
887.325	Fixed E	345.37	0.1910	861.688	351.63	333.03	18.60 kg (5.59%)

Table 3 indicates that multi-body optimization always results in a larger mass delivered at Mercury capture. The largest improvement of 13% occurs around the flight time of 857.325 days.

Tables 4 summarizes the results when the Venus flyby date is free for optimization. The Venus flyby date is optimized separately for the two-body and the multi-body Mercury capture. The flyby dates are expected to be different for multi- and two-body capture formulations. Freeing the flyby date removes any bias toward one formulation or the other resulting from a particular fixed flyby date.

Table 4

EARTH LAUNCH - VENUS FLYBY - MERCURY CAPTURE
Launch Date Fixed and Venus Flyby Date Free

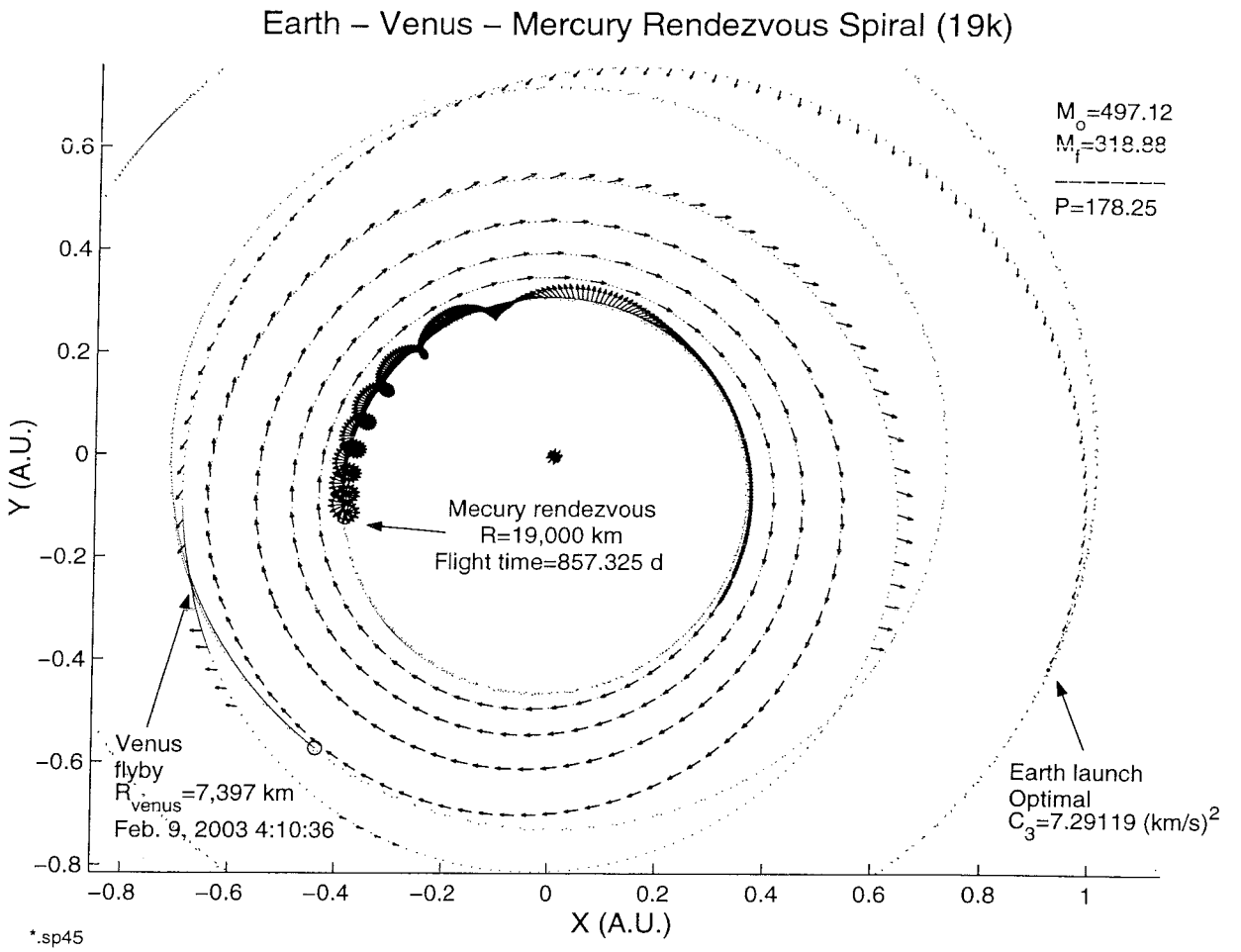

Figure 4: SDC optimal trajectory for the Earth launch to Venus flyby to Mercury orbit insertion. The target orbit around Mercury is circular with a radius of 19,000 km. The arrows along the spacecraft trajectory indicate the thrust direction. The lack of arrows along the trajectory indicate coasting periods.

Time of Flight (d)	Mercury Orbit Type	Final Mass (kg)	Final Orbit ϵ	Capture Day	Capture Mass (kg)	2-Body Capture Mass (kg)	Multi-body Optimization Improvement
847.325	Circular	319.44	0	826.745	324.47	289.81	34.66 kg (12.0%)
847.325	Fixed E	320.06	0.2844	827.122	325.00	290.30	34.70 kg (12.0%)
857.325	Circular	334.65	0	835.473	339.99	301.54	38.45 kg (12.8%)
857.325	Fixed E	334.77	0.2470	835.459	340.11	301.52	38.59 kg (12.8%)
887.325	Circular	351.47	0	861.402	357.80	332.85	24.95 kg (7.50%)
887.325	Fixed E	351.52	0.2513	861.080	357.93	332.56	25.37 kg (7.63%)

Table 4 indicates that the base case Venus flyby date (February 11, 2003) is slightly biased torwards the multi-body formulation for flight times 847.325 and 857.325 days because the relative performance of the multi-body formulation (last column) is better in Table 3 than in Table 4. However, the base case flyby date is biased torwards the two-body formulation for the 887.325 day flight time. Table 4a compares the optimal Venus flyby date and altitude for each formulation. Table 4a indicates that the difference between the two-body rendezvous and the multi-body capture increases with the flight time. The number in the Venus flyby date column specifies the last digits of the Julian Date 2,452,xxx.xxxx. For the longest flight time, the multi-body optimal Venus flyby date and radius are more than ten days later and 1,500 km higher than the two-body results. This demonstrates the sensitivity of the Venus flyby to the Mercury capture model - despite the fact that the Mercury capture occurs 700 days and 4.5 revolutions around the Sun after the Venus flyby. The existence of this sensitivity highlights the importance of using a multi-body capture model for the accurate optimization of the Earth to Mercury trajectory.

Table 4a

EARTH LAUNCH - VENUS FLYBY - MERCURY CAPTURE

Launch Date Fixed and Venus Flyby Date Free

Time of Flight (d)	Mercury Orbit Type	Venus Flyby Date	Venus Flyby radius (km)
847.325	Circular	679.0515	7,435.4594
847.325	Fixed E	679.2873	7,402.8275
847.325	Two-body	672.0684	7,163.8497
857.325	Circular	683.3509	7,248.4580
857.325	Fixed E	683.3476	7,251.5866
857.325	Two-body	674.4275	7,471.2007
887.325	Circular	693.3322	9,008.4964
887.325	Fixed E	693.3820	9,005.6482
887.325	Two-body	682.7581	7,473.1845

The difference between the multi-body circular orbit and multi-body fixed energy results in Tables 4 and 4a are small for fixed flight times. The difference grows slightly when the flight time is more constrained. The similarity of results indicates that the Venus flyby parameters and over-all performance are not sensitive to the shape of the Mercury target orbit for eccentricities between 0 and 0.3.

Table 5 summarizes the results when both the launch date and Venus flyby date are free for optimization. Only the final arrival date is fixed. Freeing both the launch and flyby date removes

any bias toward one particular formulation. The multi-body capture results optimize both launch and the Venus flyby for the multi-body capture. The two-body solutions optimize both the launch and Venus flyby for the two-body capture formulation. The two-body optimization uses a fixed arrival date equal to the corresponding multi-body capture date.

Table 5

EARTH LAUNCH - VENUS FLYBY - MERCURY CAPTURE
Launch Date Free and Venus Flyby Date Free

Arrival Date	Mercury Orbit Type	Final Mass (kg)	Final Orbit ϵ	Time of Flight (d)	Capture Mass (kg)	2-Body Capture Mass (kg)	Multi-body Optimization Improvement
12.24.04	Circular	320.16	0	863.220	325.20	290.68	34.52 kg (11.9%)
12.24.04	Fixed E	320.76	0.2843	862.779	325.71	291.28	34.43 kg (11.8%)
1.3.05	Circular	335.13	0	868.451	340.48	302.37	38.11 kg (12.6%)
1.3.05	Fixed E	335.25	0.2484	868.425	340.60	302.36	38.24 kg (12.6%)
2.2.05	Circular	352.33	0	894.826	358.66	333.12	25.54 kg (7.67%)
2.2.05	Fixed E	352.37	0.2312	894.808	358.77	332.85	25.92 kg (7.79%)

Table 5 demonstrates that even when both the launch and Venus flyby are optimized separately for each formulation, the performance of the multi-body capture is still nearly 13% better than the two-body capture. Table 5a compares the optimal launch date and Venus flyby parameters for each formulation. The two-body and multi-body launch date, launch C_3, Venus flyby date, and radius differ by as much as 5 days, 2.5 $\frac{km^2}{s^2}$, 14 days, and 1000 km respectively.

Table 5a

EARTH LAUNCH - VENUS FLYBY - MERCURY CAPTURE
Launch Date Free and Venus Flyby Date Free

Arrival Date	Mercury Orbit Type	Launch Date	Launch C_3 ($\frac{km^2}{s^2}$)	Venus Flyby Date (km)	Venus Flyby radius
12.24.04	Circular	500.2800	-6.8152	672.9315	9,229.2140
12.24.04	Fixed E	500.7208	-6.7911	673.2774	9,183.3512
12.24.04	two-body	499.1950	-9.3150	663.4840	8,286.4606
1.3.05	Circular	505.0486	-6.0148	680.8927	8,444.7613
1.3.05	Fixed E	505.0751	-6.0073	680.9158	8,445.9924
1.3.05	Two-body	499.3135	-8.1002	666.4311	8,995.3090
2.2.05	Circular	508.6744	-5.3480	691.3054	9,491.4400
2.2.05	Fixed E	508.6917	-5.3472	691.3548	9,491.3368
2.2.05	Two-body	510.9248	-6.2652	681.3673	8,055.3965

Earth Launch to Venus Capture Spiral

The mass of Venus greatly exceeds that of Mars and Mercury so it is expected that the difference between multi-body and two-body capture optimization will be significantly larger for Venus verses Mars and Mercury. To test this hypothesis, a Venus capture trajectory problem was constructed.

The Earth launch to Venus capture problem uses a fixed arrival date in a circular orbit around Venus of October 18, 2004. The flight time varied from 206 days to 289 days. The launch vehicle used is a Delta 7326-9.5 with a 7% launch vehicle contingency. The launch V_∞ direction and magnitude is free for optimization. Two NSTAR 30-cm ion thrusters are available on the spacecraft. The solar array power available to the engines at 1 A.U. is 4.0 kW. This array allows both engines to operate at full power (184.4mN at 5.2 kw) anywhere below a heliocentric radius of 0.821 A.U. The target orbit at Venus is a circular orbit with a radius of 100,000 km. The multi-body results are compared to the optimal two-body rendezvous. The optimal two-body rendezvous uses the same launch date and flight time to capture as the corresponding optimal multi-body result. For example, for a flight time is 246 days, the optimal trajectory to a circular orbit around Venus uses 246 days but achieves capture on day 202.46. A comparison is made to the optimal two-body capture using the same launch date and a fixed flight time of 202.46 days. The two-body problem is based on a massless Venus and the constraint Eq. (14).

A typical optimal multi-body Venus orbit insertion is plotted in Figure 5. Figure 6 is the capture portion of the same trajectory centered on Venus. The final orbit in Figure 6 does not appear circular because the orbit is inclined and the trajectory is projected onto the ecliptic.

Figures 7 and 8 compare the multi-body mass delivered to the two-body mass delivered to capture. Figure 7 is a plot of the mass delivered verses flight time to capture at Venus. The multi-body optimization mass delivered (upper line) is significantly greater than the two-body mass delivered (lower line). Figure 8 is a plot of the percent improvement in mass delivered to capture by multi-body optimization compared to two-body optimization. The maximum improvement of 30% is obtained near a flight time of 165 days. The maximum improvement of for Mercury capture was 13% and for Mars capture it was 20%. The bumpy-ness of the two-body performance in Figure 7 occurs because the launch and flight time used for two-body optimization is the launch and capture time in the corresponding multi-body optimization. The slope changes in the two-body curve are due to new coasting periods appearing in the multi-body solution that make the progression of the launch and capture times non-smooth.

Mars Escape Spiral to Earth Capture Spiral

A Mars escape to Earth capture problem illustrates the that at least two local minima exist in the the capture problem. The Mars escape to Earth capture trajectory begins in orbit around Mars on April 15, 2005. The initial Mars orbit has eccentricity of .05, a semi-major axis of 45,000 km, and an inclination of 5^o relative to the ecliptic. The spiral at Mars changes little between test cases. Some Mars spirals include a short coast, some do not, but all have the same number of revolutions to escape. Figure 9 is a plot of a typical Mars escape spiral. The spiral to escape Mars is used as a plausible trajectory origin (Mars sample return), but was not the central focus of this investigation. The focus of this investigation is on the capture into the Earth system. The target orbit at Earth was either a captured orbit with a fixed periapsis of 100,000 km or an orbit with a fixed, negative final energy of -1.4 $\frac{km^2}{s^2}$. Figure 10 is a plot of a typical complete trajectory. The initial spacecraft mass in Mars orbit is 500 kg. The solar array power available to the thrusters is 11 kw at 1 A.U. Two NSTAR 30-cm ion thrusters are available on the spacecraft. The total flight time is varied between 295 and 390 days.

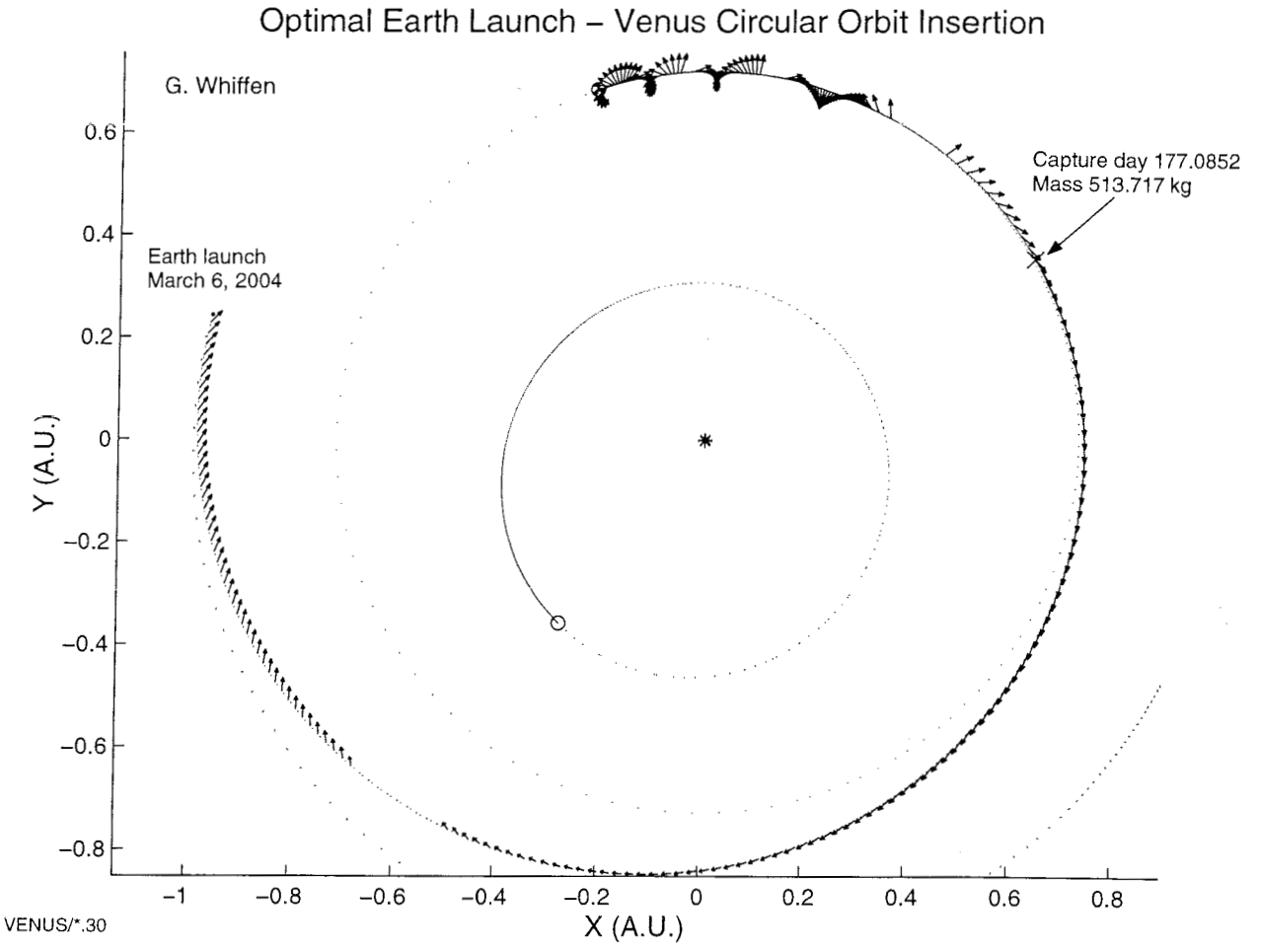

Figure 5: An example of an optimal trajectory for the Earth launch to Venus circular orbit insertion problem. The arrows along the spacecraft trajectory indicate the thrust direction. The lack of arrows along the trajectory indicate coasting periods.

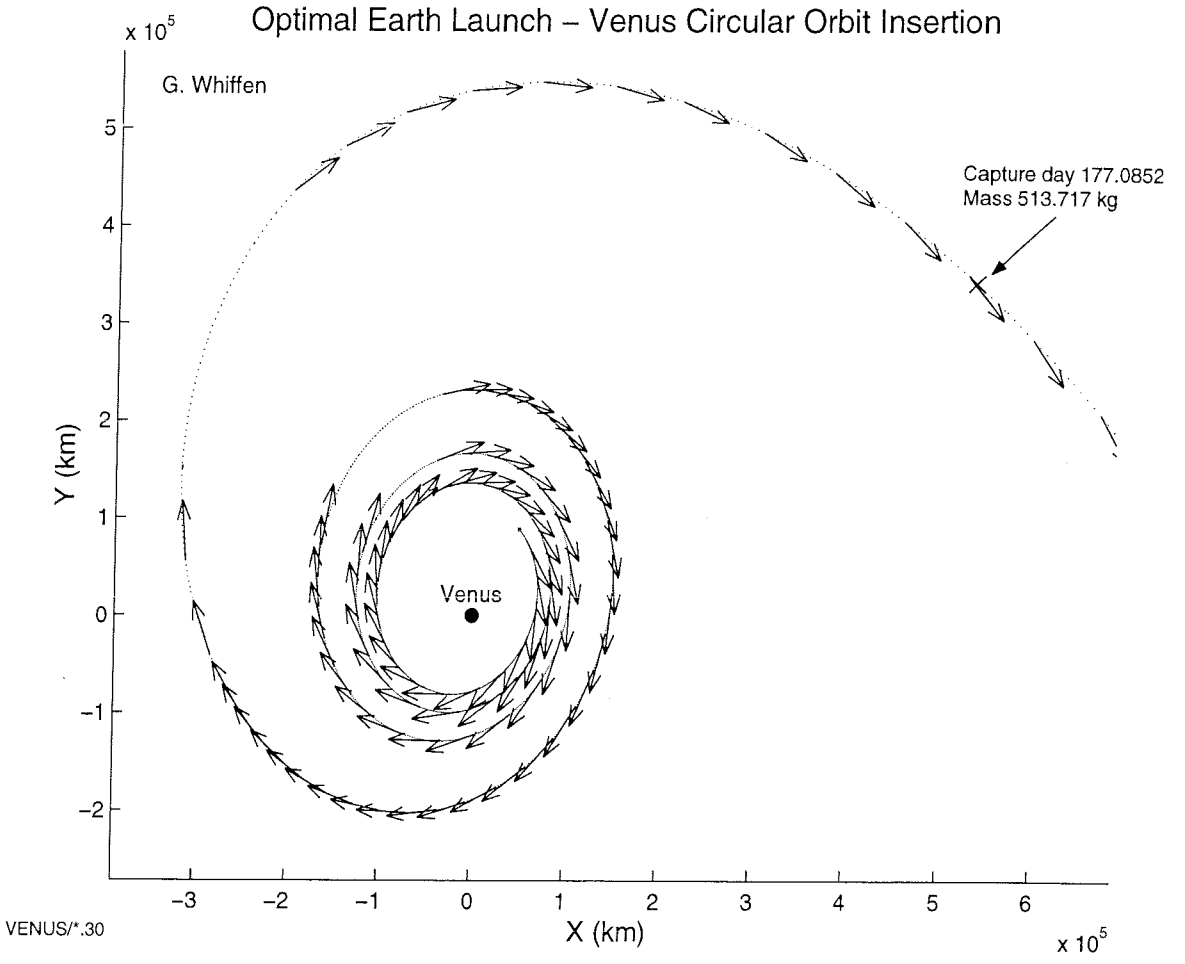

Figure 6: An example of an optimal trajectory for the Earth launch to Venus circular orbit insertion problem. This plot is centered on Venus to show detail of the capture and circular orbit insertion. The trajectory is projected onto the ecliptic.

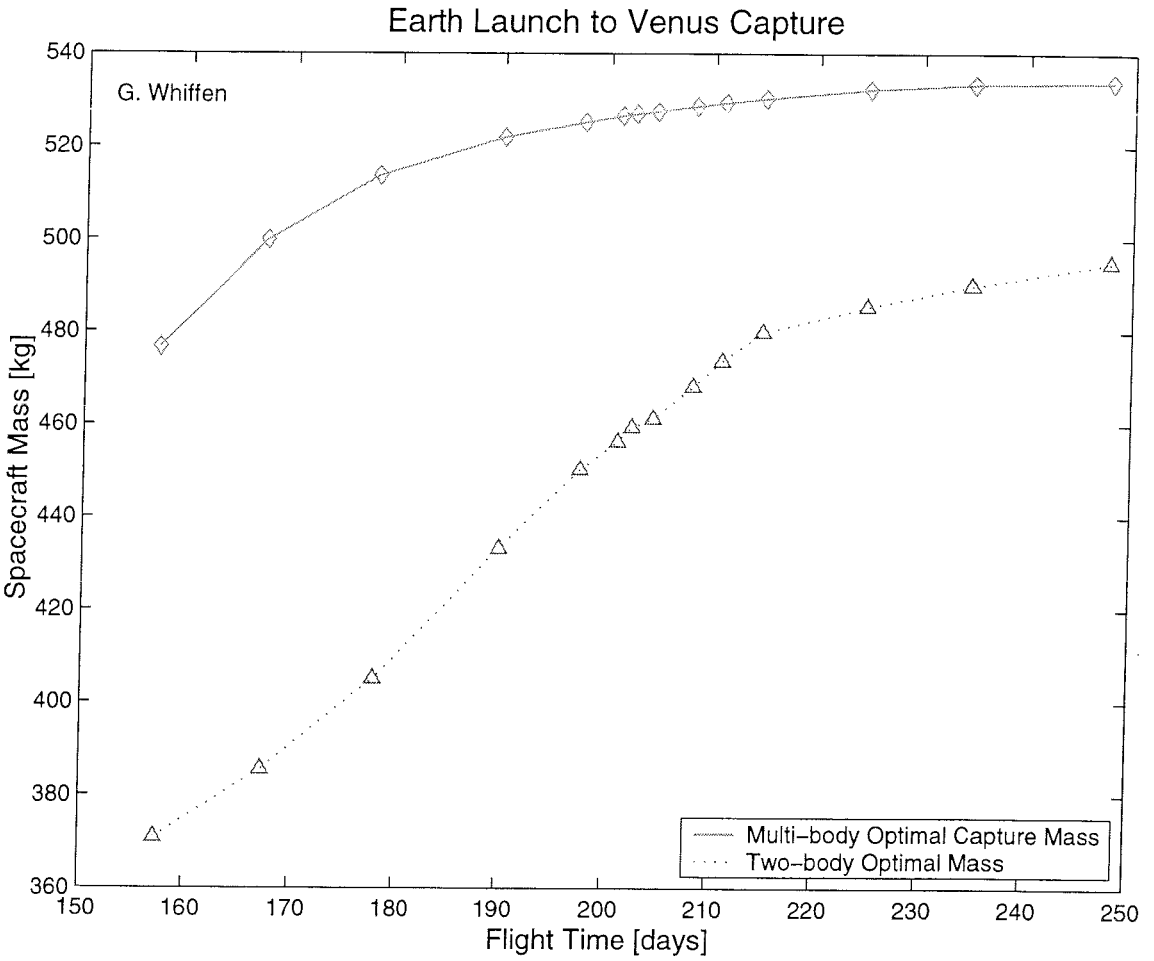

Figure 7: Comparison of SDC optimal multi-body verses two-body mass delivered for the Earth launch to Venus circular orbit insertion problem.

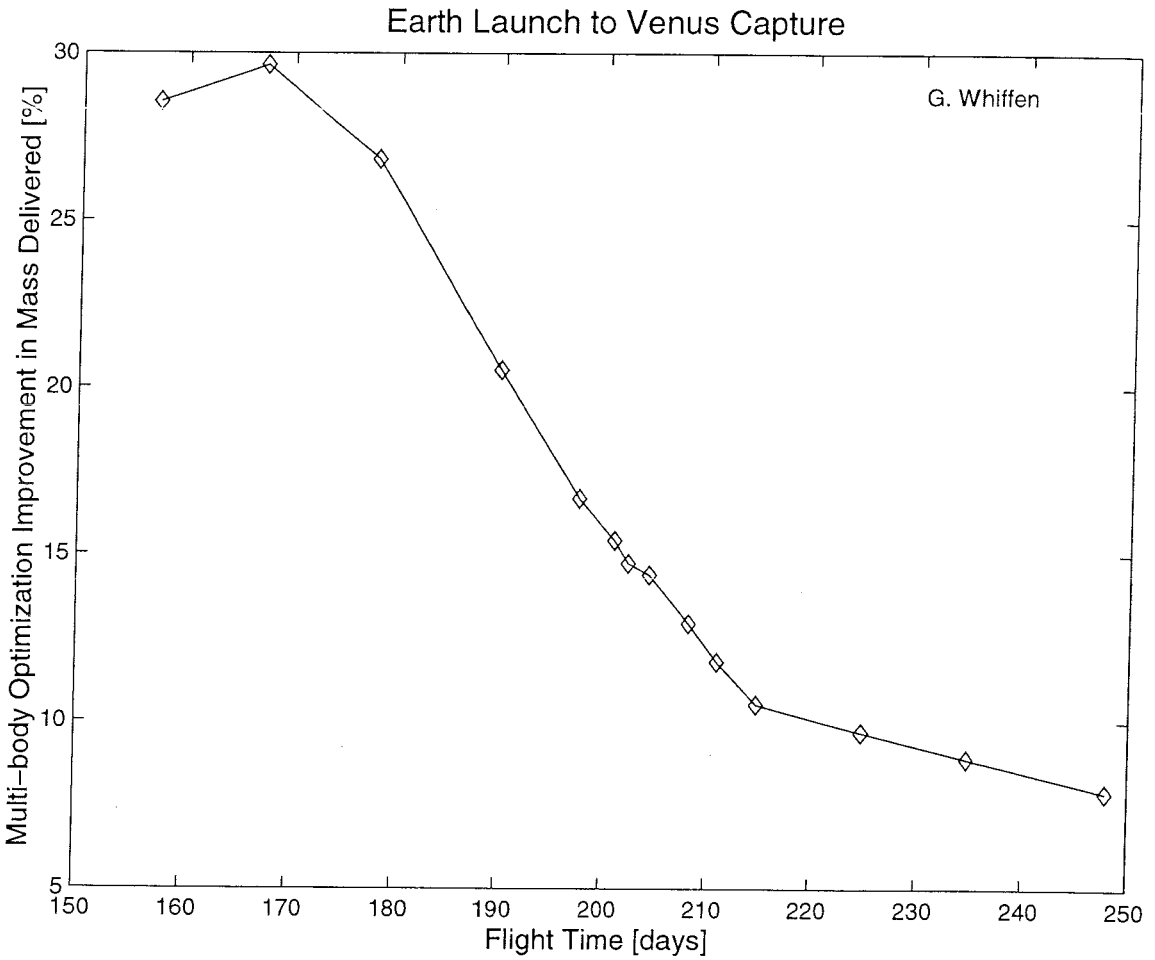

Figure 8: Percent improvement of optimal multi-body mass delivered verses two-body mass delivered for the Earth launch to Venus circular orbit insertion problem.

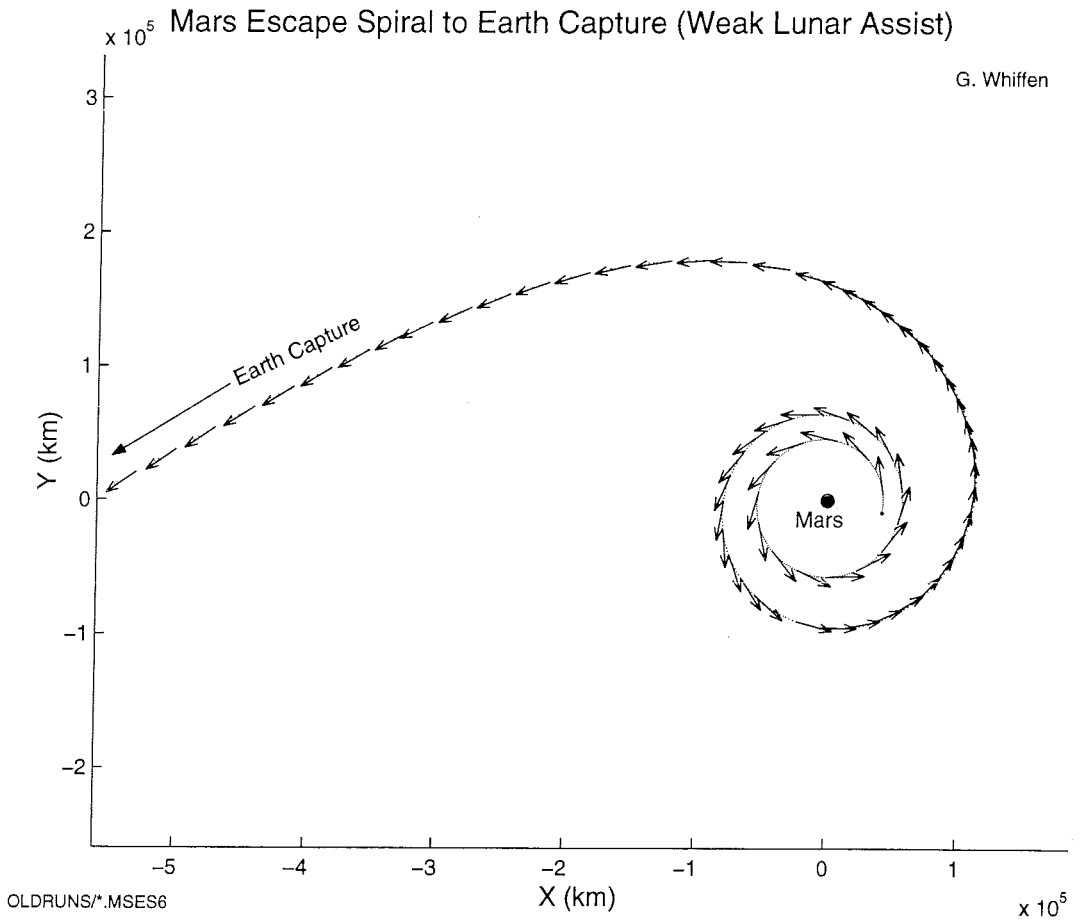

Figure 9: An example of the Mars spiral portion of a typical Mars escape to Earth capture trajectory.

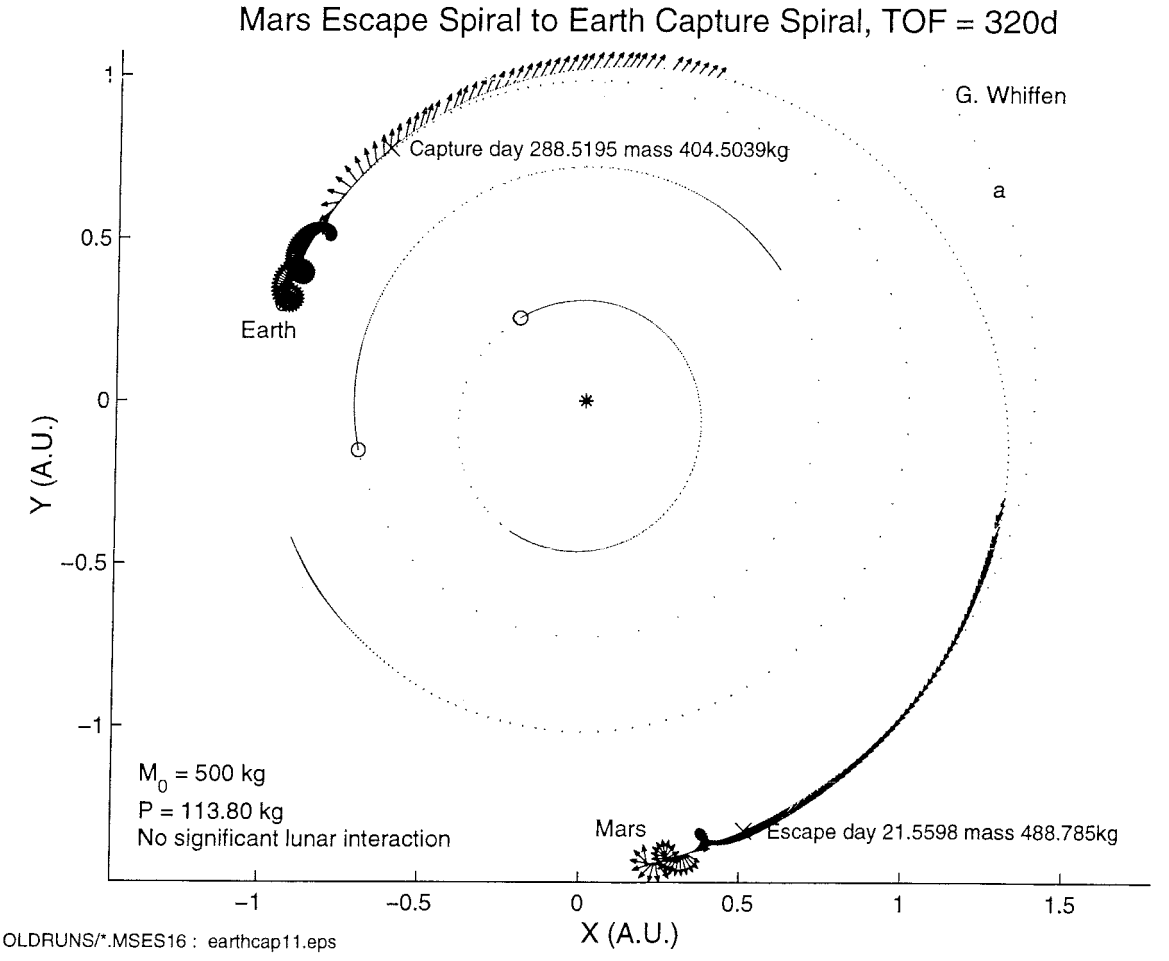

Figure 10: An example of a complete Mars escape to Earth capture trajectory.

Three-body Capture

A series of optimal Mars escape spiral to Earth capture spiral trajectories were generated using SDC. This series assumes the Earth is gravitating but the Moon is not (three-body capture problem). Four body capture (Moon gravitating) is the subject of an upcoming paper. The target orbit at Earth is constrained to have an energy of -1.4 $\frac{km^2}{s^2}$.

There are at least two basic classes of optimal captures for flight time limited (TOF $<$ 385 days) three-body capture. One minima type has a high final Earth orbit eccentricity and the other minima type has a low final orbit eccentricity. The relative superiority of the minima types depends on the allowed flight time. An example of a low eccentricity type Earth capture is plotted in Figure 11. Minima of this type are characterized by continuous engine operation throughout the capture and spiral. Figure 12 is a plot of a typical high eccentricity minima. Thrust arcs roughly centered on the periapsis characterize this type of trajectory.

For long flight times (in excess of 385 days) the variety of high eccentricity type minima increases. For shorter flight times there seems to be a single high eccentricity minima for each flight time. The number of revolutions at the Earth begins at 2.5 for the shortest possible flight times and steadily increases to, and plateaus at, 2.75. When the flight time is long enough, there is freedom to add additional revolutions to the capture at Earth, and change the approach. Two examples are provided in Figures 13 and 14. The trajectory plotted in Figure 13 has a similar initial approach (inside the Moon's orbit) as short flight time, high eccentricity minima. The only difference is the initial capture orbit is much larger and the trajectory involves 3.5 revolutions of the Earth. The trajectory in Figure 14 has a very different initial approach, far outside the orbit of the Moon.

Figure 15 is a plot of the optimal three-body performance (final mass) verses flight time. Low eccentricity minima are plotted with triangles and high eccentricity minima are plotted with squares. Stars are used to plot the two long flight-time minima corresponding to Figures 13 and 14. The relative difference between minima types for a given flight time is small. However, the ranges that different minima occur in have structure. Figure 15 indicates that for short flight times (less than 331 days), only low eccentricity solutions are obtained. This result is related to the fact that for a highly constrained flight time, the thrusters must operate nearly continuously. If the thrusters must operate continuously, then the most efficient spiral shape is as close to instantaneously circular as possible. Figure 15 indicates that for flight times between 331 days and 355 days both high and low eccentricity minima are obtained. In this flight-time range, the efficiency of the nearly circular spiral creates a minima that coexists with minima that exploit the efficiency of centering thrusting arcs around periapsis of a higher eccentricity spiral. The leftmost data point in Figure 15 represents the minimum feasible flight time trajectory according to SDC. No trajectory of this type exists for flight times less than 295.4 days. Figure 16 is a rescaling of the plot in Figure 15 to the flight-time range in which both high and low eccentricity minima coexist. Figure 16 indicates that high eccentricity minima are inferior to low eccentricity minima for flight times less than 338 days, but high eccentricity minima become superior after 338 days. The trajectory shown in Figure 11 is the longest flight time (flight time of 355 days), low eccentricity minima that was obtained. As flight time is increased, it is more and more difficult to choose an initial guess that will converge to low eccentricity minima (instead, high eccentricity minima are obtained). This can be understood because the low eccentricity minima begin superior, but become inferior to high eccentricity minima as flight time increases. It is likely that the region of influence of low eccentricity minima shrinks with increasing flight time.

Another way to look at three-body capture is to plot the spacecraft mass at the instant of capture verses the time of flight to the instant of capture. Figures 17 and 18 plot the capture mass verses the capture day for the mass-less Moon series. Notice that the difference between the low eccentricity

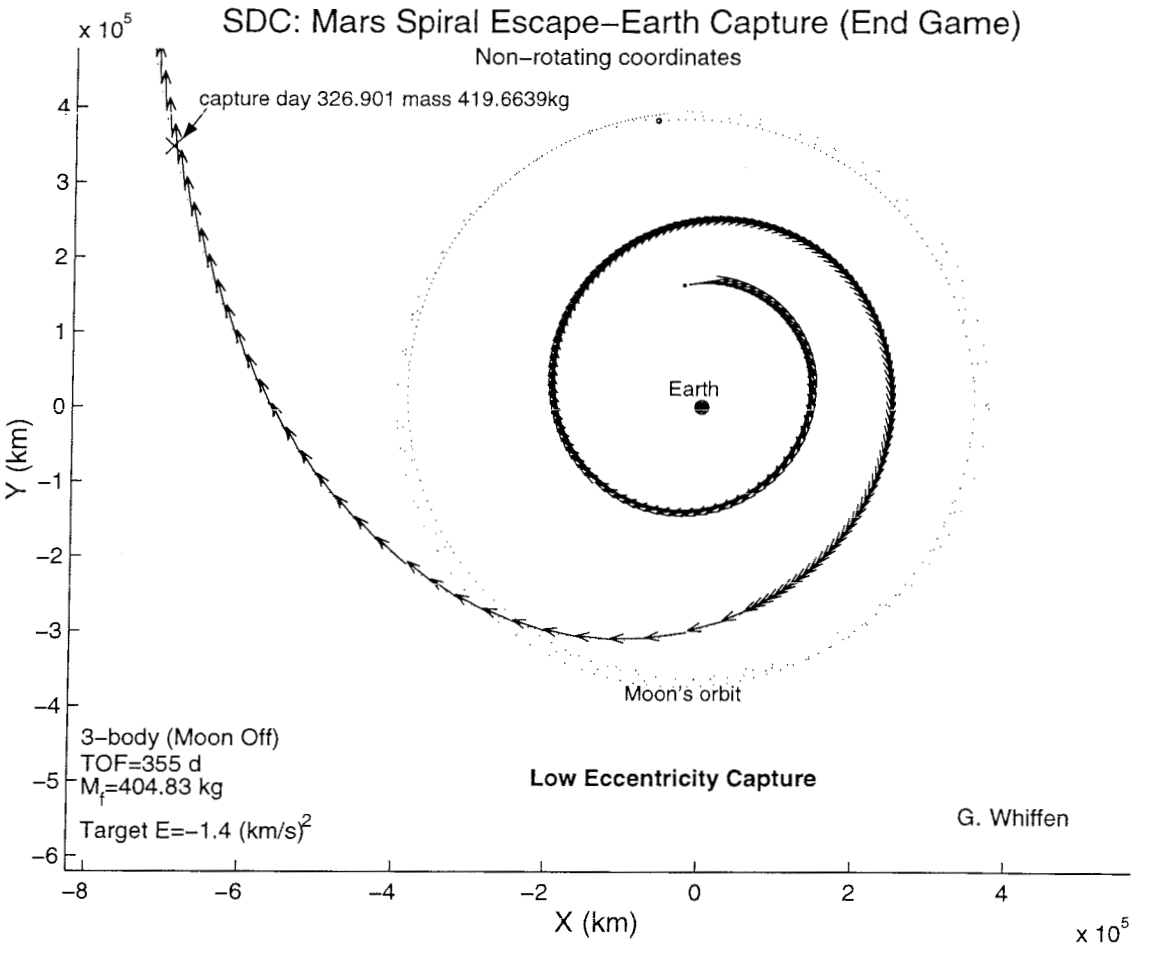

Figure 11: An example of a low eccentricity type minima for the Mars escape to Earth capture problem without the Moon gravitating (three-body problem).

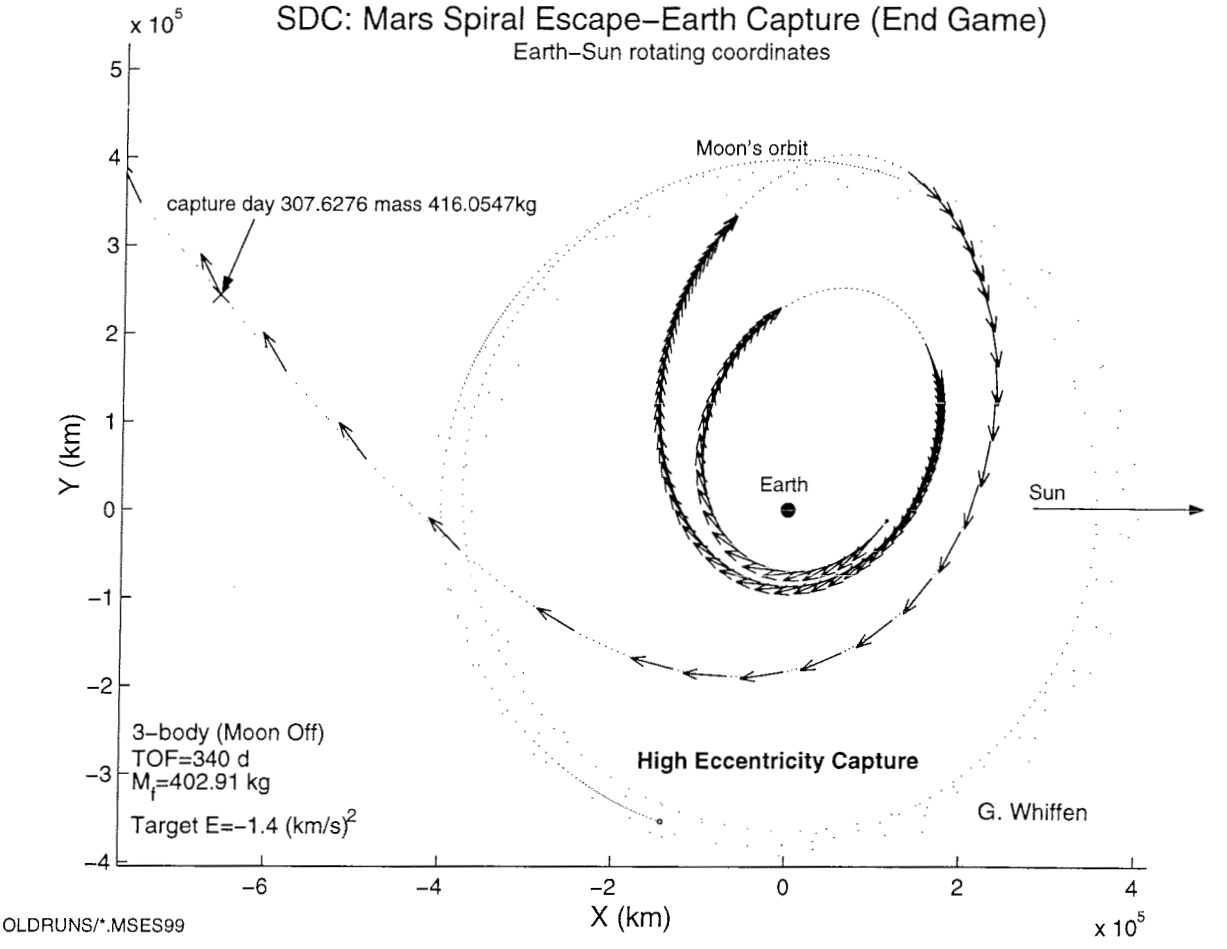

Figure 12: An example of a high eccentricity type minima for the Mars escape to Earth capture problem without the Moon gravitating (three-body problem).

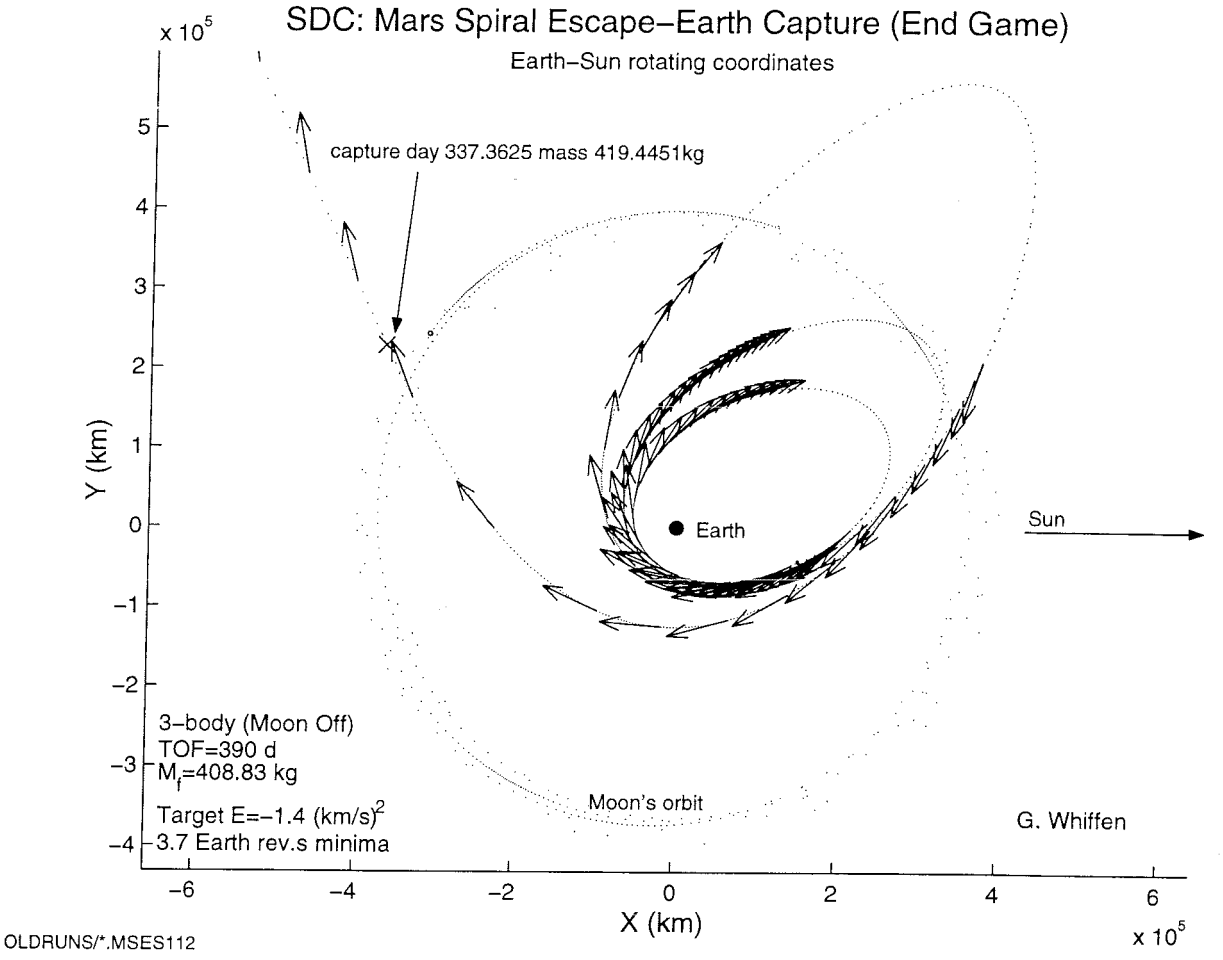

Figure 13: An example of a long flight-time high eccentricity type minima for the Mars escape to Earth capture problem without the Moon gravitating (three-body problem).

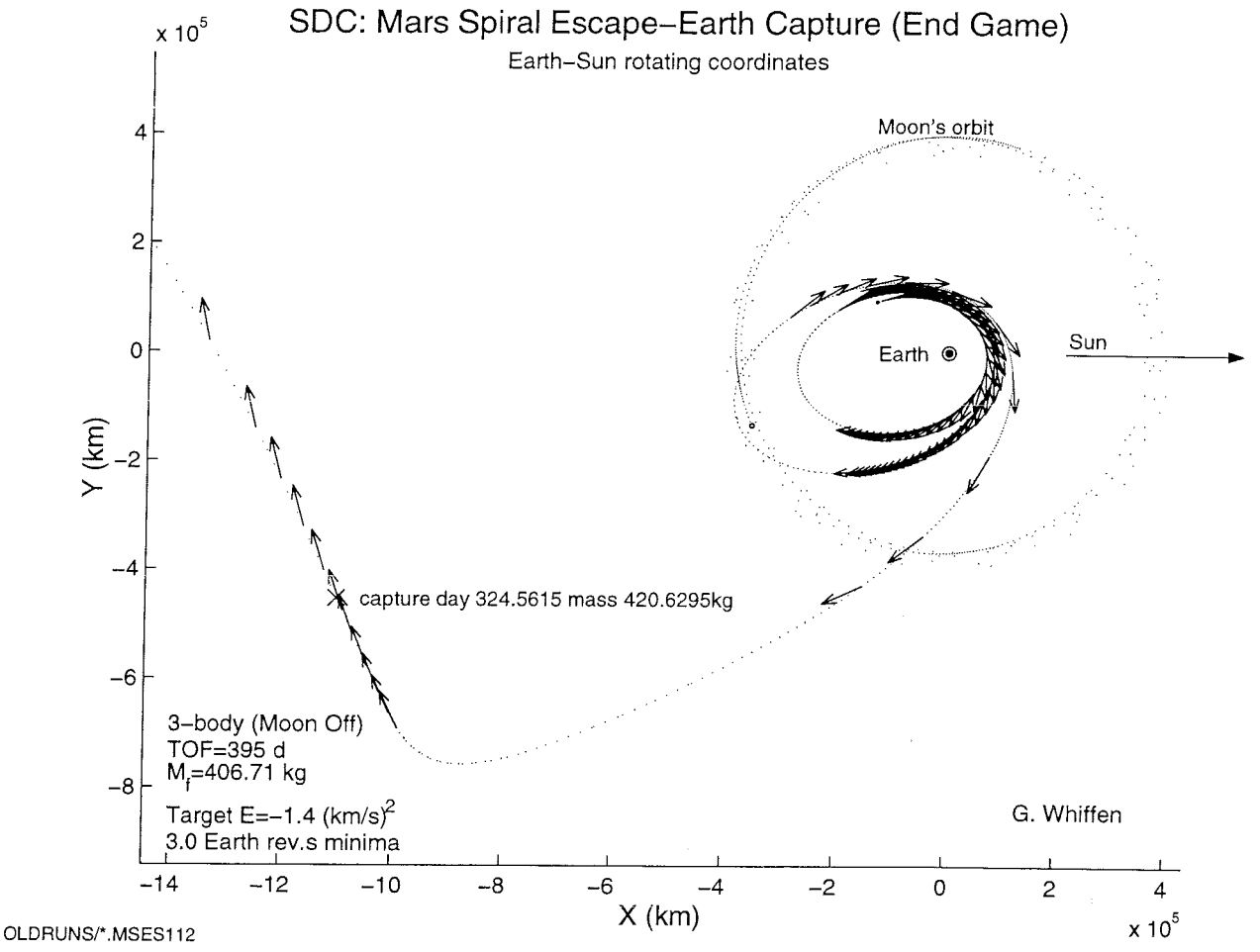

Figure 14: An example of a long flight-time high eccentricity type minima for the Mars escape to Earth capture problem without the Moon gravitating (three-body problem).

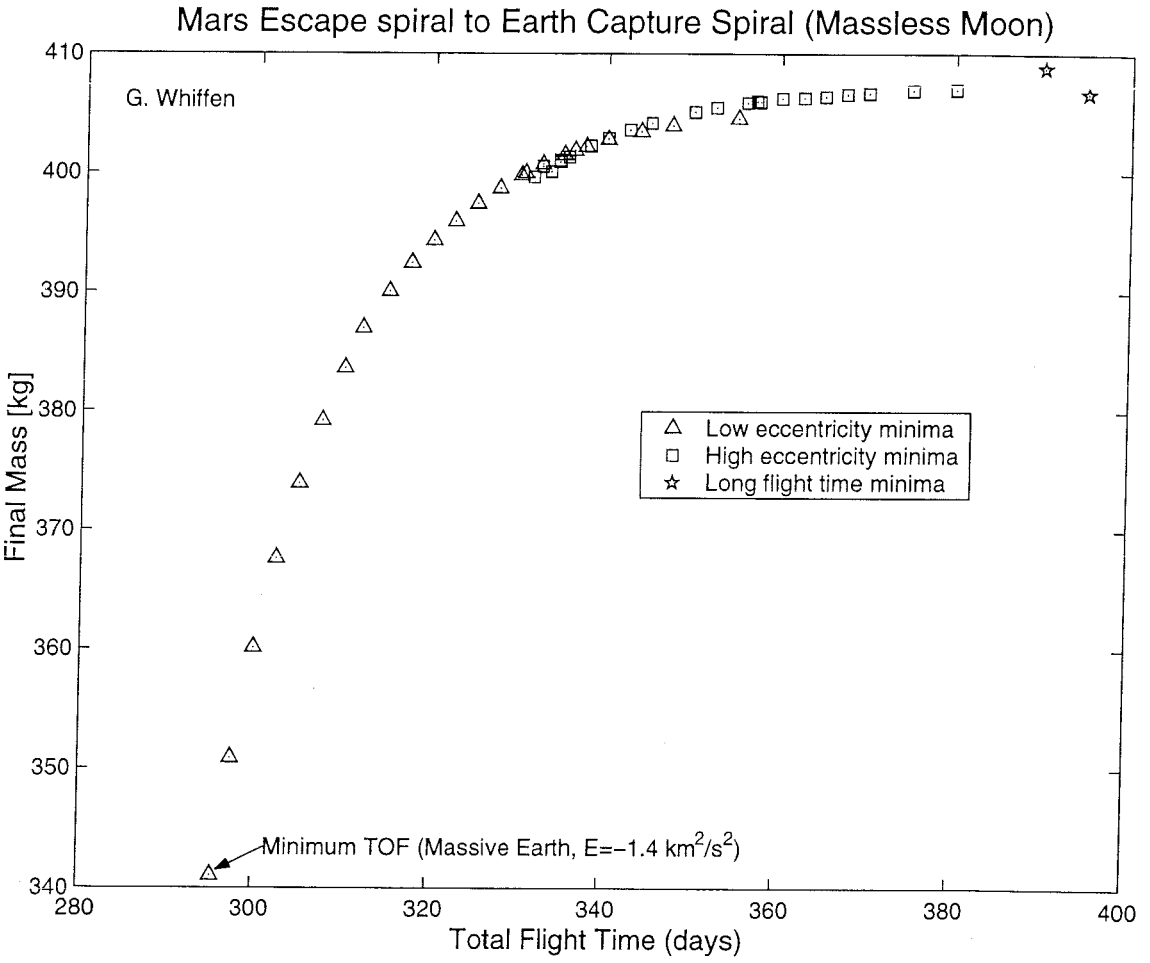

Figure 15: The optimal three-body performance (final mass) verses total flight time.

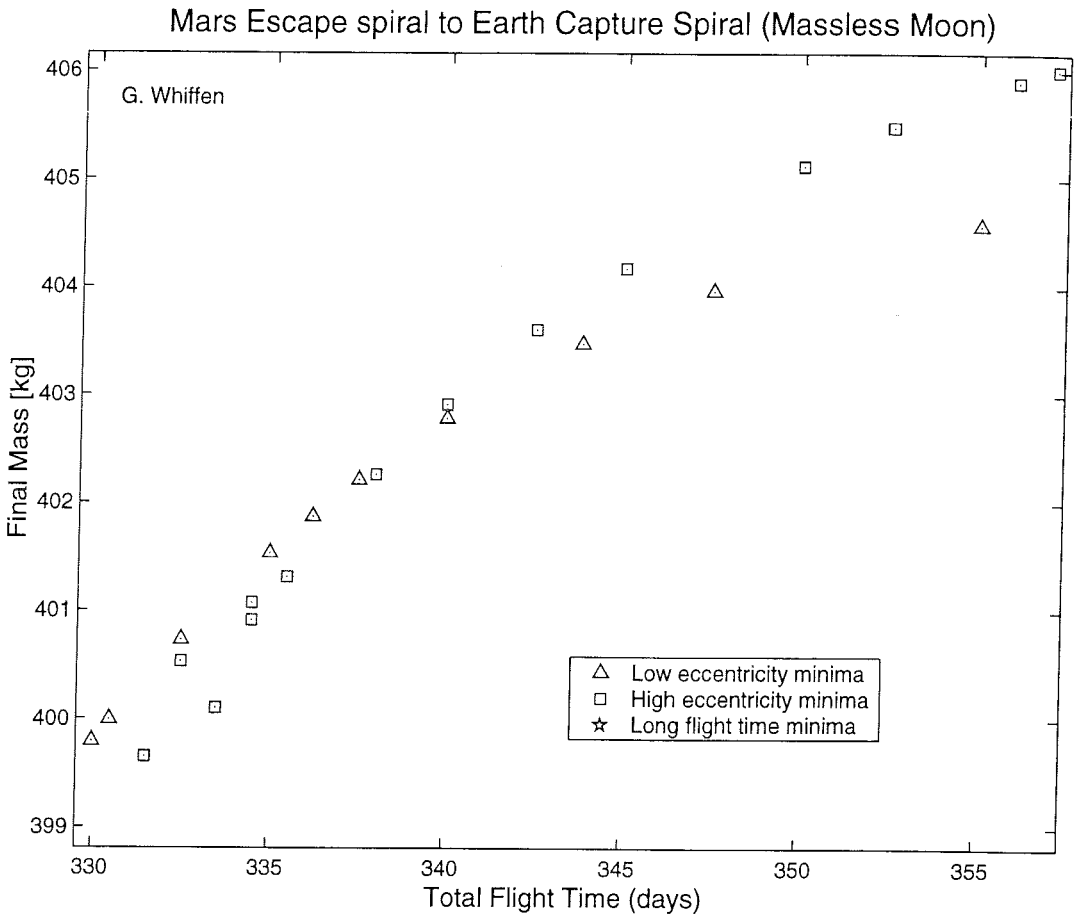

Figure 16: The optimal three-body performance (final mass) verses total flight time scaled to the flight-time range in which both high and low eccentricity minima coexist.

and the high eccentricity minima is again small. The minimum feasible flight time trajectory to a final energy of -1.4 $\frac{km^2}{s^2}$ (total flight time = 295.4 days) captures on day 273. Figure 18 is a magnified portion of the plot in Figure 17. Figure 18 shows that there is a smooth bifurcation in capture mass between the two types of minima unlike the bifurcation in final mass in Figure 16. Figures 17 and 18 show that the capture mass is always higher for low eccentricity minima, however, recall that the final mass is not always better (see Figure 16). The objective is to maximize final mass in orbit, not maximize the mass at the instant of capture. Low eccentricity minima naturally capture at higher mass. For short flight times, the higher capture mass of low eccentricity minima exceeds the advantage that high eccentricity minima have: higher efficiency thrusting during the spiral in. This is because the coasting periods near apogee of high eccentricity minima are short in response to the short over-all flight time. The efficiency of the Earth spiral after capture is illustrated in Figure 19. Figure 19 is a plot of the propellant mass fraction required from capture to reach the target final energy in Earth orbit of -1.4 $\frac{km^2}{s^2}$. The mass fraction is measured relative to the spacecraft mass at the instant of capture. The efficiency of high eccentricity spirals is always better (lower propellant mass fraction) than low eccentricity minima. The efficiency of high eccentricity spirals increases with flight time because less thrusting far from periapsis is necessary when there is more flight time freedom.

Two-body Capture

The two-body capture problem was optimized for comparison to the three-body results presented above. The two-body problem treats the Earth and Moon as massless, and the rendezvous condition Eq. (14) is used to constrain the final spacecraft position and velocity to match that of the Earth-Moon barycenter. Figure 20 is a plot combining the two- and three-body local minima. Figure 20 indicates that all multi-body minima outperform the corresponding two-body minima - which is consistent with the previous investigations in this paper. The minimum feasible flight time to capture for the two-body problem is nearly 20 days longer than the minimum three-body flight time to capture. Table 6 provides the relative improvement of multi-body optimization capture mass verses two-body optimization capture mass for various flight times to capture.

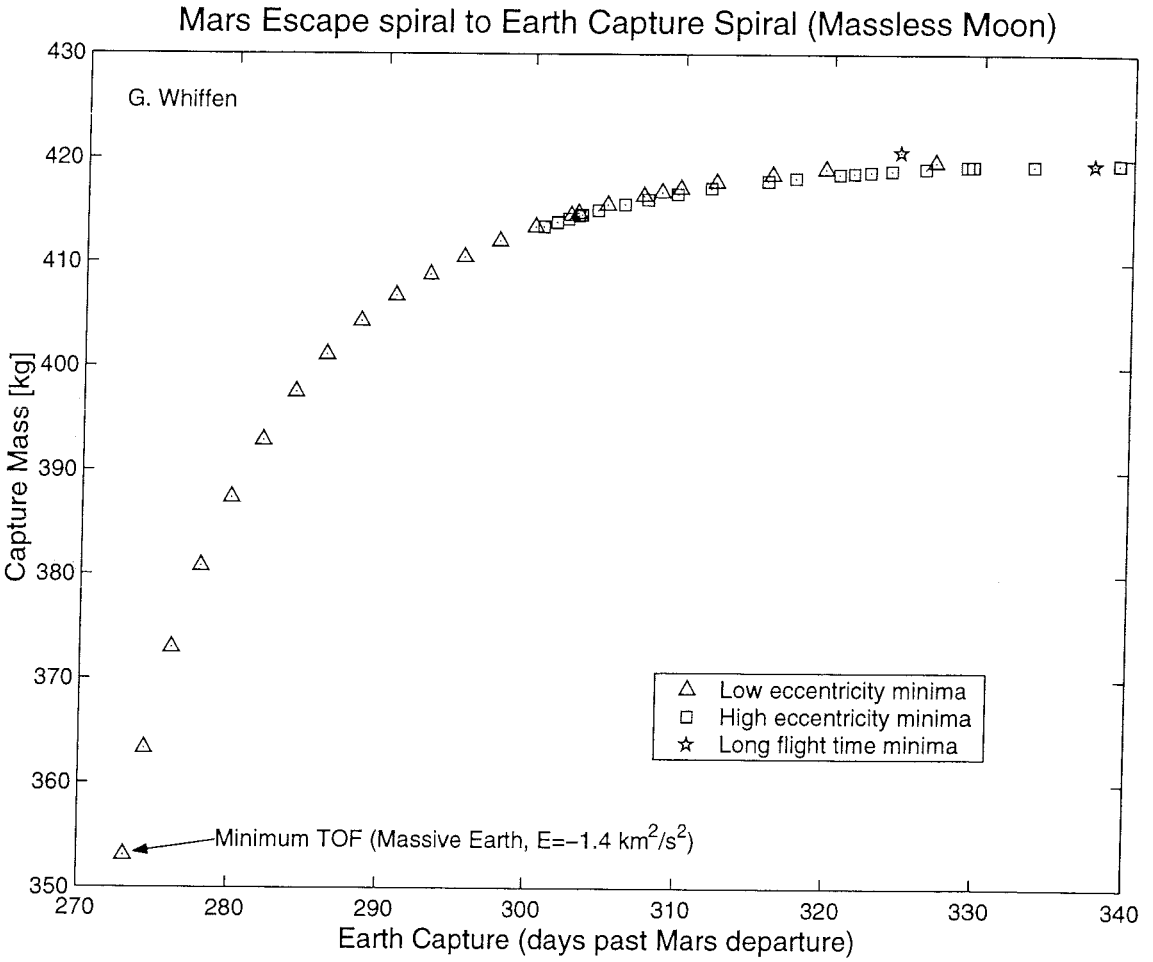

Figure 17: Capture mass verses flight time to capture for the Mars escape spiral to Earth capture spiral problem. The Earth's Moon is given zero mass (three-body capture problem).

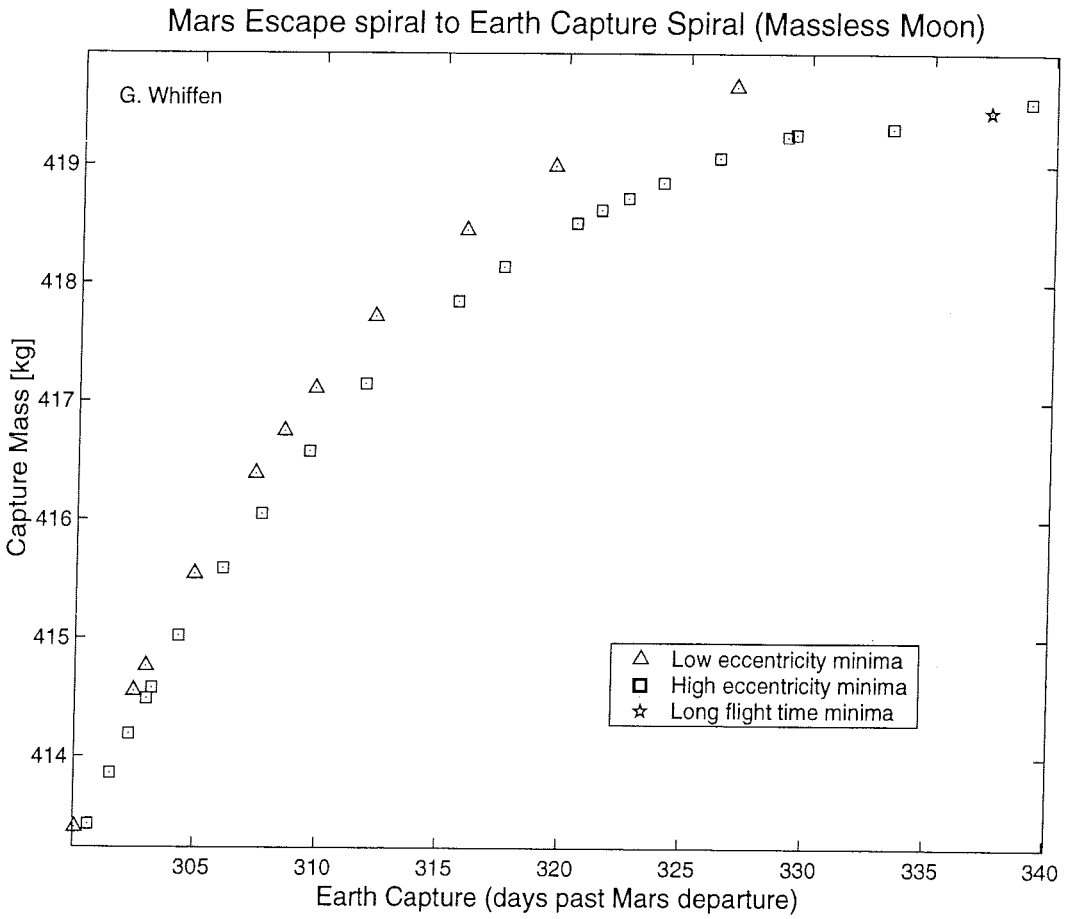

Figure 18: Capture mass verses flight time to capture for the Mars escape spiral to Earth capture spiral problem. The Earth's Moon is given zero mass (three-body capture problem). The plot is scaled to highlight the range in flight time when both high and low eccentricity minima coexist.

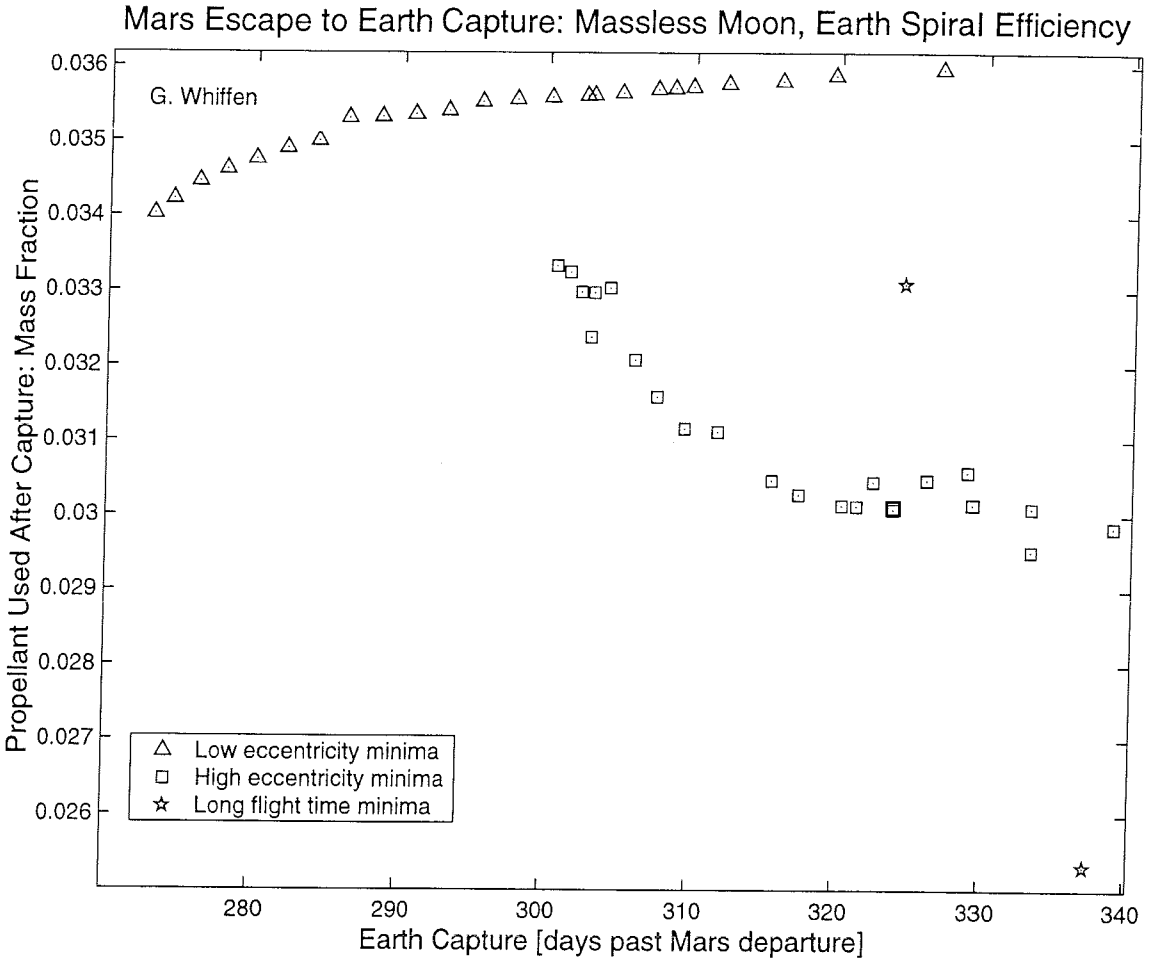

Figure 19: Mass fraction of propellant used after Earth capture to arrive in a final Earth orbit with an energy of -1.4 $\frac{km^2}{s^2}$. The mass fraction is plotted verses time of flight to Earth capture. The mass fraction is measured relative to the spacecraft mass at the instant of capture.

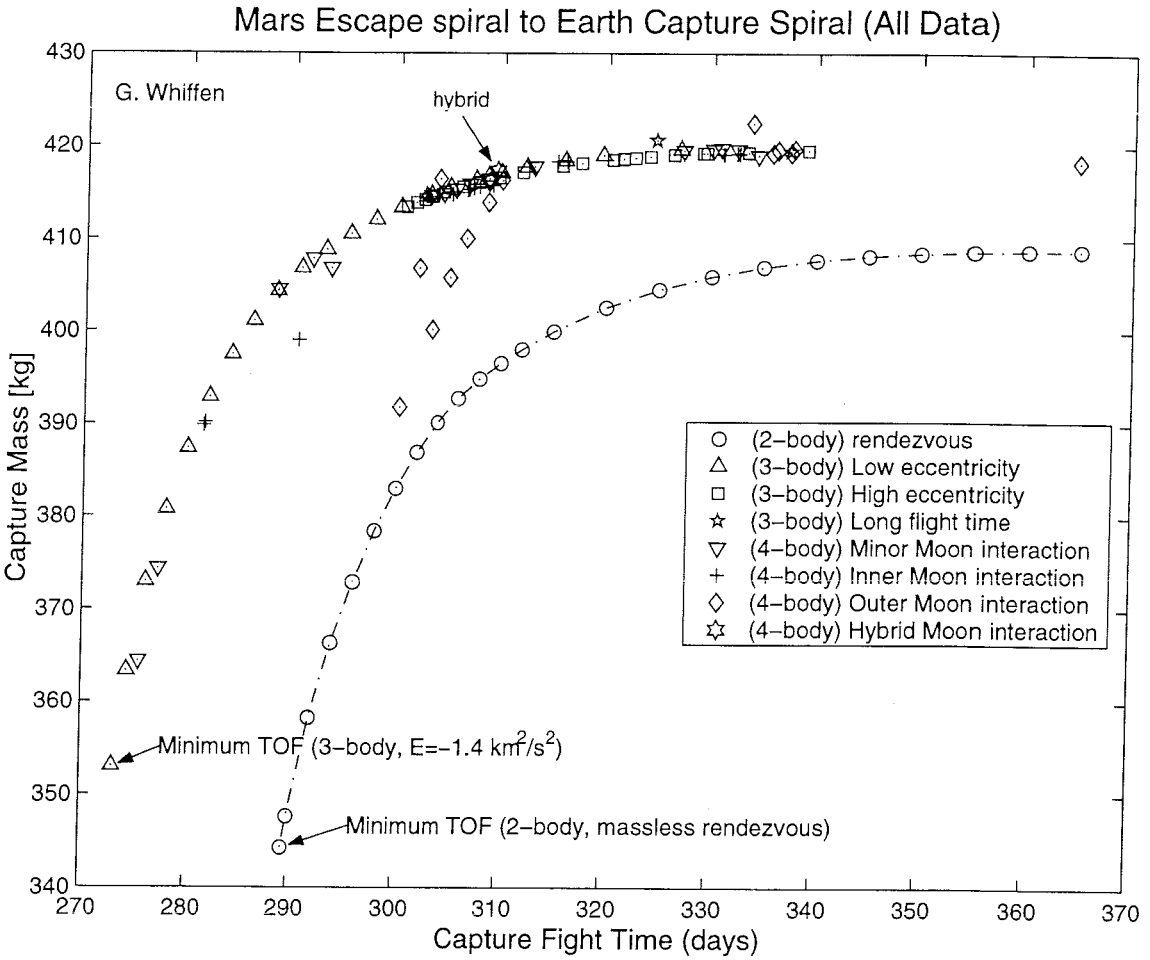

Figure 20: A plot of capture flight time to capture mass for all four-, three-, and two-body minima.

Table 6

MARS ESCAPE TO EARTH CAPTURE

Flight Time to Capture (days)	Optimal Multi-body Capture Mass (kg)	Optimal Two-body Capture Mass (kg)	Improvment Over Two-body Capture
333.80	422.44	406.71	15.70 kg 3.9%
315.20	418.30	400.05	18.30 kg 4.6%
291.82	407.82	357.28	50.54 kg 14.1%
289.50	406.00	344.28	61.72 kg 17.9%
281.61	390.14	INFEASIBLE	390.14 kg ∞%

CONCLUSION

Using Lunar Interactions for Earth Escape and Capture

The remander of this paper will focus on using lunar interactions for both escape from Earth and capture at Earth.

The capture problems discussed up to this point can be classified as "three-body" problems. The significant gravitating bodies during capture are the Sun and the plant at which capture is occurring. All other planets are gravitating, but their influence during capture is very small. Escape and capture in the Earth-Moon system can accordingly be classified as a "four-body" problem because the list of significant gravitating bodies must now include the Moon in addition to the Sun and Earth. Obviously, the four body problem generates a more complex optimization space.

SDC is uniquely suited to explore the optimal trajectories that exist in the four-body case. SDC does not require a good guess to begin the optimization. It is this feature that is used to explore the complex optima space of four-body capture and escape. A large number of poor initial guesses and different initial conditions were generated to begin separate optimizations. The purpose of this procedure is to investigate (with as little bias as possible) the range of available, locally optimal trajectories. Hundreds of different optimal escape and capture trajectories were obtained in this way. A clarification system was developed and all trajectories were classified as belonging to one of ten distinct minima types. Escape and capture exhibits a symmetry in that, capture minima often have analogous escape minima.

The relative performance of four-body optima can be compared to three-body optima by setting the Moon's mass to zero and resolving the optimization. Similarly, the multi-body solutions can be compared to the two-body solution by setting both the Earth and Moon mass to zero and using constraint Eq. (14) for a two-body capture at Earth.

CONCLUSION

SDC is robust for solving multi-body trajectory optimization problems. SDC is able to investigate the complex optimization space of capture and escape using low-thrust. SDC converges readily even when trajectories have length scale changes of over 10^4. Trajectories that involve planet centered spirals and interplanetary legs involve large changes in time and length scales. Large scale changes are known to cause difficulty for optimization methods. Linking planet centered spirals to interplanetary destinations or origins is essential for complete trajectory optimization. SDC provides a means for computing optimal trajectories that can begin in orbit around one planet and end in orbit around another planet.

The two-body formulation of rendezvous is a poor approximation to the performance of multi-body capture. Optimizing a multi-body trajectory was shown to improve performance (mass delivered) by up to 13%, 20% and 30% for the examples that capture at Mercury, Mars, and Venus respectively. In addition, two-body rendezvous models predict significantly different optimal launch, intermediate flyby, and arrival dates than does SDC with the high-fidelity multi-body capture constraints used in this research.

The capture problems analyzed in this paper can be classified as "three-body" problems. The significant gravitating bodies during capture are the Sun and the plant at which capture is occurring. All other planets are gravitating, but their influence during capture is very small. Escape and capture in the Earth-Moon system can accordingly be classified as a "four-body" problem because the list of significant gravitating bodies must now include the Moon in addition to the Sun and Earth. Obviously, the four body problem generates a more complex optimization space. SDC is uniquely suited to explore the optimal trajectories that exist in the four-body case. Upcoming papers will present the results of applying SDC to capture and escape from the Earth-Moon system.

ACKNOWLEDGEMENT

This work was supported by a NASA grant. This work was carried out by the Jet Propulsion Laboratory in Pasadena, California.

REFERENCES

1. Sauer, Carl G., Jr., "Solar Electric Performance for Medlite and Delta Class Planetary Missions," Paper AAS 97-726, AAS/AIAA Astrodynamics Specialist Conference, Sun Valley, Idaho, August 4-7, 1997.

2. Kirk, D.E. *Optimal Control Theory: An Introduction,* Prentice-Hall Inc. N.J., 1970.

3. Polk, J. E., Anderson, J. R., Brophy, J. R., Rawlin, V. K., Patterson, M. J., and Sovey, J. S., "The Effect of Engine Wear on Performance in the NSTAR 8000 Hour Ion Engine Endurance Test," Paper AIAA 97-3387, 33rd AIAA/ASME/SAE/ASEE Joint Propulsion Conference and Exhibit, Seattle, WA, July 6-9, 1997.

4. Sims, Jon A., and Flanagan, Steve N., "Preliminary Design of Low-Thrust Interplanetary Missions," Paper AAS 99-338, AAS/AIAA Astrodynamics Specialist Conference, Girdwood, Alaska, August 16-19, 1999.

5. Williams, Steven N., and Coverstone-Carroll, Victoria, "Benefits of Solar Electric Propulsion for the Next Generation of Planetary Exploration Missions," *Journal of the Astronautical Sciences*, Vol. 45, No. 2, April-June 1977, pp. 143-159.

6. Gill, Philip E., Murray, Walter, and Saunders, Michael A., "User's Guide for SNOPT 5.3: A FORTRAN Package for Large-Scale Nonlinear Programming."

7. Vadali, S. R., Nah, R., Braden, E., and Johnson, I. L. Jr., "Fuel-Optimal Planer Earth-Mars Trajectories Using Low-Thrust Exhaust-Modulated Propulsion," Journal of Guidance, Control, and Dynamics, Vol. 23, No. 3, May-June, 2000.

8. Whiffen, Gregory J., and Sims, Jon A., "Application of a Novel Optimal Control Algorithm to Low-Thrust Trajectory Optimization," Paper AAS 01-209, AAS/AIAA Astrodynamics Specialist Conference, Santa Barbara , California, February 11-14, 2001.